



A sequential addition and migration method for generating microstructures of short fibers with prescribed length distribution

Alok Mehta¹ · Matti Schneider¹

Received: 18 February 2022 / Accepted: 8 June 2022
© The Author(s) 2022

Abstract

We describe an algorithm for generating fiber-filled volume elements for use in computational homogenization schemes. The algorithm permits to prescribe both a length distribution and a fiber-orientation tensor of second order, and composites with industrial filler fraction can be generated. Typically, for short-fiber composites, data on the fiber-length distribution and on the volume-weighted fiber-orientation tensor of second order is available. We consider a model where the fiber orientation and the fiber length distributions are independent, i.e., uncoupled. We discuss the use of closure approximations for this case and report on identifying the describing parameters of the frequently used Weibull distribution for modeling the fiber-length distribution. We discuss how to integrate these procedures in the Sequential Addition and Migration algorithm, developed for fibers of equal length, and work out algorithmic modifications accounting for possibly rather long fibers. We investigate the capabilities of the introduced methodology for industrial short-fiber composites, demonstrating the rather low dispersion of the effective elastic moduli for the generated unit cells.

Keywords Short-fiber composite · Representative volume element · Fiber-length distribution · Weibull distribution · Sequential addition and migration

1 Introduction

1.1 State of the art

Due to their favorable stiffness-to-weight ratio, fiber-reinforced composites are frequently used when designing lightweight components. When a high design freedom is required, injection molding with discontinuously reinforced polymers is typically the first choice. Due to the anisotropy of the fiber reinforcements, the effective mechanical properties of such fiber-reinforced composite materials are anisotropic, as well. Moreover, as a consequence of the complex manufacturing process, the material microstructure varies throughout the component. For instance, the fiber-volume fraction, the fiber orientation and also the fiber-length distribution may are typically subject to non-homogeneity.

To improve upon the predictive capability of mean-field models [1–3], computational homogenization techniques [4]

are typically employed to determine the effective mechanical properties of such composites. Based on the mathematical theory of homogenization [5,6], computational homogenization represents a well-defined and flexible strategy to understand the influence of the constituents and the microstructural composition on the effective mechanical properties which complements the pertinent experimental procedures in an effective way.

Modern image-processing techniques provide a detailed impression about the complexity of fiber-reinforced materials [7,8]. To reduce the the influence of randomness and to keep the number of parameters manageable, microstructure-generation tools [9] are highly valuable prerequisites for accurate computational multiscale modeling procedures. For short-fiber composites, the fibers do typically show little bending, and an approximation by a straight cylinder is appropriate. Simple algorithms based on random sequential addition (RSA) [10,11] fail to produce microstructures with industrial volume fraction and moderate fiber aspect-ratio, i.e., the quotient of fiber length and diameter, and this limitation is intrinsic [12,13]. Therefore, a number of improved RSA methods was introduced [14–17]. Sequential deposition [18,19], flexible fiber based [20,21] and collec-

✉ Matti Schneider
matti.schneider@kit.edu

¹ Institute of Engineering Mechanics, Karlsruhe Institute of Technology (KIT), Karlsruhe, Germany

tive re-arrangement algorithms [22–24] are more successful when it comes to reaching the desired volume fractions. As a particular example of the latter group, the sequential addition and migration (SAM) method [25] was shown to generate short-fiber microstructures with straight cylinders and high fiber-volume fractions. Moreover, a fourth-order fiber-orientation tensor could be prescribed to the SAM algorithm, and the produced microstructure was shown to match the prescribed orientation tensor to high accuracy. This close match of a number of pre-defined statistical desirables implied that different computational cells produced closely matching effective mechanical properties. Even more striking, the size of the considered unit cells could be chosen to be extremely small, and still be representative [26–28]. Such a property is extremely desirable, in particular when it comes to nonlinear material properties of composites, and turned out to be critical when undertaking a number of scientific studies, including fatigue [29,30], fracture [31,32] and thermomechanically coupled problems [33,34].

1.2 Contributions

This work is concerned with an extension of the SAM method [25] to fibers of variable length, preserving the positive characteristics of the method shown for constant fiber lengths. Such an augmentation is less trivial than one might think initially. The challenges are actually twofold. The first, more obvious challenge, concerns the presence of very long fibers in unit cells. The classical SAM method [25] required the cell size to exceed the fiber length. If we retained this prerequisite, the cell would have to be larger than the longest considered fiber. In particular, such an approach would be computationally inefficient. Alternatively, we need to account for fibers that are longer than the cell edge-length. As we consider periodic boundary conditions, such a fiber may wrap around the cell several times, as shown in Fig. 1. In particular, it may intersect itself. Appropriate strategies are required to reliably deal with such a situation.

The second challenge is more subtle, and concerns the statistical data to be prescribed, balanced by the actual data that is available. Indeed, although micro-computed tomography (μ CT) scans of fiber composites are readily available, extracting the full fiber length-orientation distribution from voxel data is far from trivial. Indeed, algorithms for segmenting individual fibers from voxel data are still subject of the latest research [35], yet only detect around 80% of the fibers. Thus, we need to live with the available data. For extracting the length-weighted fiber-orientation tensors of second and fourth order from voxel data, reliable algorithms are available [36–38]. Moreover, the fiber-length distribution may be

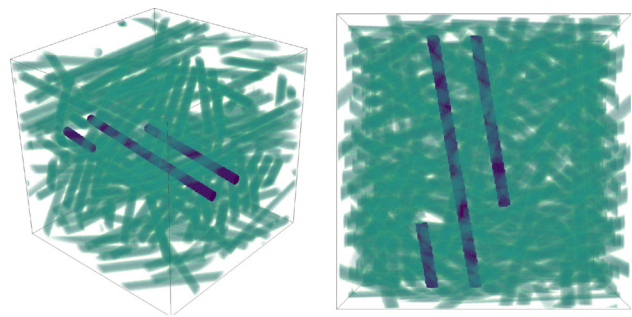


Fig. 1 An example of a unit cell with edge length of $200\mu\text{m}$; a single rather long fiber of length $392.9\mu\text{m}$ is highlighted

determined from classical incineration (see Tab. 1 in Goris et al. [39]).

For the work at hand, we assume that the fiber orientation and the fiber-length distribution are independent. Recent experimental data [40] suggests that there is a coupling between fiber length and fiber orientation, yet only weakly so. In particular, our working assumption may be a good starting point, in particular in view of the data available. We consider the volume-weighted fourth-order fiber-orientation tensor as the target statistical quantity. In the computational experiments, it turns out that prescribing this statistical quantity indeed keeps the statistical fluctuations rather low for the considered scenario.

For concreteness, we consider the Weibull distribution [41] for modeling the statistics of fiber lengths, as it was shown previously to accurately model length data of short fibers [42–44]. We introduce a strategy to determine the governing parameters from prescribed (volume-weighted) mean length and its standard deviation, which appears to be innovative. Moreover, we introduce a quasi-random based strategy to sample the fiber lengths, minimizing stochastic artifacts in the process.

This work is organized as follows. Section 2 introduces the players of our game in a mathematically precise context, i.e., fiber-length and orientation distributions, the Weibull distribution and the relevant closure approximations for the fiber-orientation tensor. The algorithmic counterparts concerning the sampling of both length as well as orientation and the required modifications of the SAM algorithm are described in sect. 3. We demonstrate the capabilities of the introduced procedures in sect. 4 for a commercial PA6GF35, studying the necessary resolution, RVE (representative volume element) size and the influence of the mean as well as standard deviation of the length distribution on the effective elastic moduli. Moreover, we validate the approach with published experimental data [40]. The appendices provide details for determining the Weibull parameters and shed light on the similarities and differences of the exact and the maximum-entropy closure.

2 Describing short-fiber microstructures

2.1 Fiber-orientation and fiber-length distributions

We consider short-fiber reinforced composites, i.e., we assume that each fiber in such a composite may be described by a straight cylinder with length ℓ , principal axis p and diameter d . Typically, the variations of the diameter between different fibers of a composite is negligible, whereas both the fiber length ℓ and the fiber orientation p vary significantly. The latter two characteristics may be described in terms of a length-orientation distribution function

$$\psi : \mathbb{R}_{>0} \times S^2 \rightarrow \mathbb{R}_{\geq 0}, \quad (\ell, p) \mapsto \psi(\ell, p), \quad (2.1)$$

where S^2 denotes the unit sphere in \mathbb{R}^3 . The length-orientation distribution function is a probability distribution which satisfies the symmetry condition

$$\psi(\ell, p) = \psi(\ell, -p) \quad \text{for all } \ell > 0 \quad \text{and } p \in S^2, \quad (2.2)$$

which reflects the sign ambiguity when describing a cylinder in terms of its principal axis.

In practice, the full length-orientation distribution function ψ is not known, and only partial information and estimates are available. A classical way to estimate the fiber-length distribution $\rho : \mathbb{R}_{>0} \rightarrow \mathbb{R}_{\geq 0}$,

$$\rho(\ell) = \int_{S^2} \psi(\ell, p) dS, \quad \ell > 0, \quad (2.3)$$

proceeds via incineration of the matrix material (see Tab. 1 in Goris et al. [39]), and counting the fiber length of the individual fibers under the microscope. In particular, the connection between fiber length and orientation is lost.

Fiber-orientation data is typically encoded via fiber-orientation tensors [45,46], which can be determined from μ CT images [36–38,47,48]. Fiber-orientation tensors correspond to moments of the length-orientation distribution ψ , and the two most popular fiber-orientation tensors are of second and fourth order,

$$\begin{aligned} A &= \int_0^\infty \int_{S^2} \ell p \otimes p \psi dS d\ell \Big/ \int_0^\infty \ell \rho d\ell \quad \text{and} \\ \mathbb{A} &= \int_0^\infty \int_{S^2} \ell p \otimes p \otimes p \otimes p \psi dS d\ell \Big/ \int_0^\infty \ell \rho d\ell \end{aligned} \quad (2.4)$$

Fiber-orientation tensors have their roots in injection-molding simulations where the second-order fiber-orientation tensor A is often the only information available [49,50]. Although considering higher moments in the length variable ℓ is conceivable, the length-averaged form (2.4) is

the most natural, as it corresponds to a volume averaging of the cylinders. In particular, this form typically arises when computing fiber-orientation tensors from μ CT images [51].

Classically, for short-fiber reinforced composites, the details of the fiber-length distribution are ignored, and only the mean fiber length $\bar{\ell}$ is considered (with different possibilities to determine this mean). Put differently, the fiber-length distribution ρ is assumed to be concentrated at the specific fiber length $\bar{\ell}$. In this case, the fiber-orientation distribution

$$\varphi : S^2 \rightarrow \mathbb{R}_{\geq 0}, \quad p \mapsto \varphi(p), \quad (2.5)$$

carries all relevant information about the length-orientation characteristics of the composite.

Apparently, there is a gap between the data which is available and the data which would be necessary for estimating the effective mechanical properties of short-fiber composites. More precisely, (at least) three shortcomings are evident from the discussion.

1. The length-orientation distribution function (2.1) is usually unavailable. The latest computational algorithms [35,52–54] identify only about 80% of the fibers, leaving incomplete statistical information. Rather, data on the fiber-length and the fiber-orientation distributions is available separately.
2. Experimental data on the fiber-length distribution (2.3) is usually presented by counting and binning [42,44,55]. Such results are typically rather sensitive to the size of the bins with a significant influence on statistical quantities of interest, like mean and standard deviation.
3. Only rather partial information is available on the fiber-orientation tensor in terms of the second-order fiber-orientation tensor (2.4).

In this manuscript, we deal with these challenges from an engineering perspective. To deal with the first item, we make the *working assumption* that the fiber-length and the fiber-orientation distribution are uncoupled, i.e., the length-orientation distribution (2.1) may be written in product form

$$\psi(\ell, p) = \rho(\ell) \varphi(p) \quad (2.6)$$

in terms of a fiber-length distribution (2.3) and a fiber-orientation distribution (2.5). Mathematically speaking, the random variables ℓ and p are assumed to be *independent*.

From a physical point of view, it appears plausible that there is some coupling between the fiber length and the fiber orientation. Indeed, for longer fibers to arrange properly at high volume fractions, it is advantageous to align, at least locally, whereas a high degree of orientational dispersion is possible for the shorter fibers. However, for short fibers, these differences of the orientation distribution for different fiber

lengths is not very pronounced [35, Fig. 14]. In particular, our assumption appears reasonable as a working assumption.

To deal with the second item on the list of challenges, we consider specific fiber-length distributions to be able to work with a concise description of the fiber-length distribution. For the work at hand, we consider the Weibull distribution [41], which was found to be a flexible and accurate model for describing fiber-length distributions in short-fiber composites [42,43]. The details comprise sect. 2.2.

Last but not least, the use of fiber-orientation tensors is standard in injection molding, and the independence assumption (2.6) permits us to conclude

$$\int_0^\infty \int_{S^2} \ell p^{\otimes k} \psi(\ell, p) dS d\ell = \int_0^\infty \ell \rho(\ell) d\ell \int_{S^2} p^{\otimes k} \varphi(p) dS, \quad k = 0, 2, 4, \dots, \tag{2.7}$$

i.e., the expressions for the fiber-orientation tensors (2.4) simplify to expressions,

$$A = \int_{S^2} p \otimes p \varphi(p) dS \quad \text{and} \\ \mathbb{A} = \int_{S^2} p \otimes p \otimes p \otimes p \varphi(p) dS, \tag{2.8}$$

that are familiar from investigations with only a single fiber length. In particular, the fiber-orientation closure-approximation technology [56–58] developed for this scenario becomes available, see sect. 2.3. Indeed, going beyond the independence assumption (2.6) for the length-orientation distribution requires innovative closure techniques to be developed, and represents a promising research field for future contributions.

2.2 The Weibull distribution

The Weibull probability distribution [41] has been used frequently to model the fiber-length distribution in short-fiber composites [40,42,43]. Its density function [59, eq. (4-43)] reads

$$\rho_{\lambda,k}(\ell) = \frac{k}{\lambda} \left(\frac{\ell}{\lambda}\right)^{k-1} e^{-(\ell/\lambda)^k}, \quad \ell > 0, \tag{2.9}$$

where k and λ are positive parameters known as the the shape and scale parameter. The shape parameter k is sometimes referred to as Weibull modulus and is dimension-free. The scale parameter λ has dimensions of length for the model at hand. In practice, it is often more convenient to prescribe elementary statistical quantities instead of the parameters k and

λ . For instance, it would be possible to prescribe the (number-weighted) mean μ and standard deviation σ , defined via

$$\mu = \int_0^\infty \ell \rho_{\lambda,k}(\ell) d\ell \quad \text{and} \\ \sigma^2 = \int_0^\infty (\ell - \mu)^2 \rho_{\lambda,k}(\ell) d\ell, \tag{2.10}$$

and to determine the Weibull parameters λ and k . In engineering practice, it is more common to work with volume-weighted quantities instead of number-weighted ones. For the problem at hand and with the assumption of cylindrical fibers with equal diameters, the volume-weighted mean m and standard deviation s are given by the expression

$$m = \frac{1}{\mu} \int_0^\infty \ell^2 \rho_{\lambda,k}(\ell) d\ell \quad \text{and} \\ s^2 = \frac{1}{\mu} \int_0^\infty (\ell - m)^2 \ell \rho_{\lambda,k}(\ell) d\ell. \tag{2.11}$$

For given (positive) values of m and s , the parameter k solves the equation

$$\frac{\Gamma(1 + \frac{1}{k}) \Gamma(1 + \frac{3}{k})}{\Gamma(1 + \frac{2}{k})^2} = 1 + \frac{s^2}{m^2}, \tag{2.12}$$

formulated in terms of Euler’s Γ -function

$$\Gamma(z) = \int_0^\infty t^{z-1} e^{-t} dt, \tag{2.13}$$

defined for general complex numbers z with positive real part. Once Eq. (2.12) is solved, the parameter λ is calculated from the expression

$$\lambda = m \frac{\Gamma(1 + \frac{1}{k})}{\Gamma(1 + \frac{2}{k})}. \tag{2.14}$$

A derivation of Eqs. (2.12) and (2.14) is given in Appendix A.

Examples for Weibull probability distributions are shown in Fig. 2 for varying (volume-weighted) mean and standard deviation. We observe that, for fixed mean, once the standard deviation gets too large, the probability distribution develops a pole at zero, leading to a monotonically decreasing function. In contrast, for sufficiently large standard deviation, the probability density function attains a more familiar bell-like shape.

Last but not least, let us point out that the inequality

$$\mu \leq m \tag{2.15}$$

between the number-weighted mean length μ and the volume-weighted mean length m holds for any fiber-length

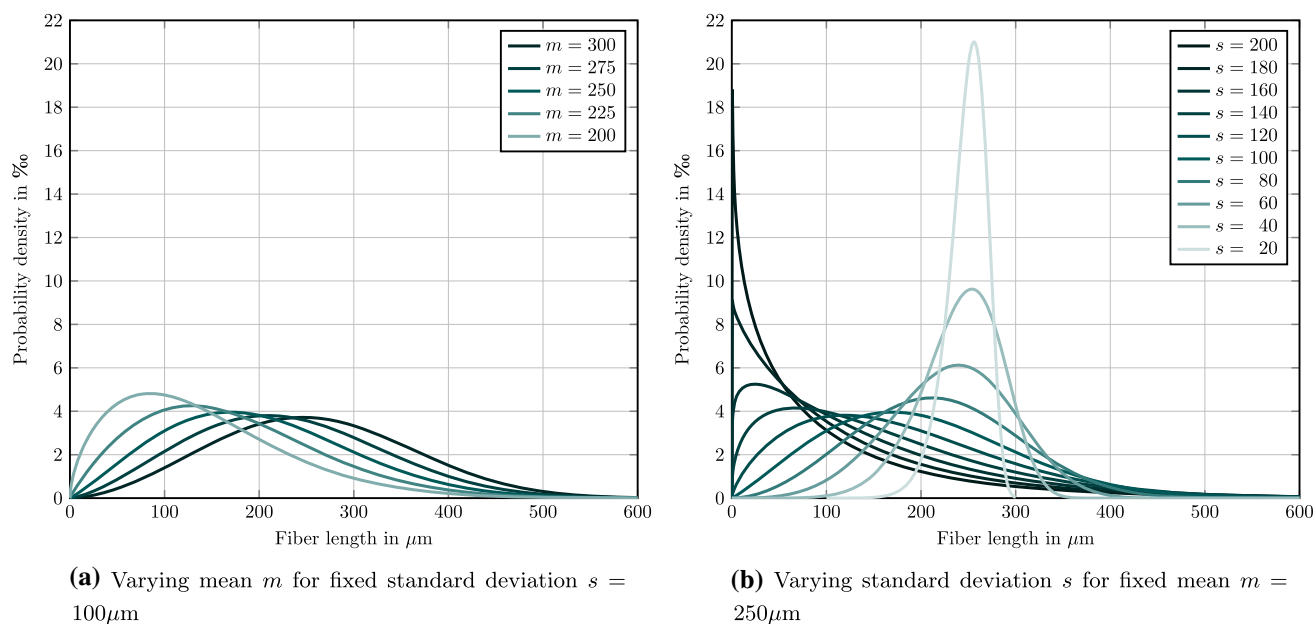


Fig. 2 Weibull probability-density functions for varying (volume-weighted) mean m and standard deviation s . **a** Varying mean m for fixed standard deviation $s = 100\mu\text{m}$. **b** Varying standard deviation s for fixed mean $m = 250\mu\text{m}$

distribution with equality only for the Dirac distribution, i.e., where all fibers have the same length. The relation (2.15) is a direct consequence of the Cauchy–Schwarz inequality

$$\int_0^\infty \ell \rho_{\lambda,k}(\ell) d\ell \leq \sqrt{\int_0^\infty \ell^2 \rho_{\lambda,k}(\ell) d\ell} \tag{2.16}$$

applied to a probability distribution.

2.3 Fiber-orientation closure approximations

When manufacturing components made of short-fiber reinforced materials the microstructure is typically varying throughout the component. In particular, the microstructure characteristics like the fiber-orientation distribution (2.5)

$$\varphi : S^2 \rightarrow \mathbb{R}_{\geq 0}, \quad p \mapsto \varphi(p), \tag{2.17}$$

vary throughout the component. Moreover, the fiber-orientation distribution contains rather fine details, which are surplus to requirements when considering process simulations and a subsequent evaluation of the mechanical properties.

Therefore, it is more convenient to work with the second- and fourth-order fiber-orientation tensors (2.8)

$$\begin{aligned} A &= \int_{S^2} p \otimes p \varphi(p) dS \quad \text{and} \\ \mathbb{A} &= \int_{S^2} p \otimes p \otimes p \otimes p \varphi(p) dS, \end{aligned} \tag{2.18}$$

introduced by Advani–Tucker [46]. Indeed, the most popular model for the evolution of the fiber orientation in fiber suspensions, the Folgar–Tucker equation [49], involves these two tensors. Moreover, it is well known that the fourth-order fiber-orientation tensor characterizes the effective elastic behavior of short-fiber composites [25,60,61], at least for fibers with uniform length.

Due to reasons of storage economy, the second-order fiber orientation tensor A is usually the primary quantity of interest, and the fourth-order fiber-orientation tensor \mathbb{A} is approximated by a so-called closure approximation [49,56,58], a tensor-valued function \mathbb{F} which establishes a relationship

$$\mathbb{A} = \mathbb{F}(A). \tag{2.19}$$

As the second-order fiber-orientation tensor may be recovered from the fourth-order fiber-orientation tensor via the relationship $\mathbb{A} : \text{Id} = A$ in terms of the 3×3 -identity Id , the information content of the fourth-order fiber-orientation tensor exceeds that of its second-order counterpart. The additional information is lost when working with a closure approximation (2.19). Yet, working with closure approximations is the rule rather than the exception [50,62,63], both for process simulations and mechanics. The success of closure approximations lies in their construction which accounts for constraints imposed by the underlying physics and selects suitable “plausible” fourth-order fiber-orientation tensors. We refer to Kugler et al. [58] for a recent review article.

The original point of view (2.19) permitted certain pathologies, which lead to unphysical or mathematically contradictory properties of the estimated higher-order tensors. For instance, the quadratic, the linear and the hybrid closure, introduced by Advani–Tucker [46], do not arise from a fiber-orientation distribution, in general.

Over time, it became apparent that it is more convenient to consider closure approximations which provide an estimate of the entire fiber-orientation distribution function φ based on prescribed fiber-orientation tensors, reducing the computation of the higher-order moments to a simple post-processing of the entire distribution function φ . The two most popular closures of this type, taking the second-order fiber-orientation tensor A as input, are the exact closure [64,65] and the maximum entropy closure [57,60].

The exact closure is based on the angular central Gaussian distribution [66]

$$\varphi_B^{\text{ex}}(p) = \frac{1}{4\pi} \left(p^T B p \right)^{-\frac{3}{2}}, \quad p \in S^2, \quad (2.20)$$

parametrized by a symmetric and positive definite 3×3 -matrix B which is moreover unimodular, i.e., satisfies $\det B = 1$. It can be shown that the ACG distributions (2.20) represent exact solutions of the fiber-orientation dynamics (with vanishing Folgar–Tucker diffusivity [49]), see Verley–Dupret [67].

The maximum entropy closure [57,60] utilizes the Bingham distribution [68]

$$\varphi_B^{\text{mE}}(p) = c_B \exp \left(p^T B p \right), \quad p \in S^2, \quad (2.21)$$

which involves a symmetric 3×3 -matrix B and a prefactor $c_B > 0$ which ensures that the total mass is one. This closure maximizes the information-theoretic entropy.

In either of the two cases, for prescribed second-order fiber-orientation tensor A , the matrix B may be determined (numerically) as a solution of the equation

$$\int_{S^2} p \otimes p \varphi_B dS \stackrel{!}{=} A. \quad (2.22)$$

Some care has to be taken if the second-order fiber-orientation tensor is singular or close to singular, i.e., the equation $\det A \ll 1$ holds [64,65,69]. In any case, with the estimated fiber-orientation distribution φ at hand, the necessary higher-order information can be post-processed, e.g., the fourth-order fiber-orientation tensor

$$\mathbb{A} = \int_{S^2} p \otimes p \otimes p \otimes p \varphi_B dS. \quad (2.23)$$

Moreover, we may draw orientation vectors from the identified distribution. The exact and the maximum entropy closure give rise to rather similar effective elastic properties for most

fiber-orientation states, see Appendix B. For the work at hand, we rely upon the exact closure approximation (2.20) due to its closer connection to the underlying physics and the simpler sampling, see sect. 3.

Let us conclude this section by discussing how to solve Eq. (2.22) for the exact closure (2.20) with a robust numerical strategy. For this purpose, integrals of the form

$$\frac{1}{4\pi} \int_{S^2} f(p) \left(p^T B p \right)^{-\frac{3}{2}} dS, \quad (2.24)$$

where $f(p)$ is a monomial in the components of the vector p , need to be evaluated. Montgomery–Smith et al. [64,65] proposed a numerical strategy to evaluate such integrals based on the Carlson form of the elliptic integrals [70]. Efficient strategies for solving eq. (2.22) based on this strategy, in particular concerning a clever initial guess, are discussed by Ospald & Herzog [69]. However, the case of degenerate fiber-orientation tensor A , i.e., whenever $\det A = 0$, requires some attention. In such a case, the fiber-orientation distribution is concentrated on a plane, and the expression (2.20) is no longer meaningful. Clearly, the special case $\det A = 0$ can be handled explicitly, see Görthofer et al. [71], for elaboration. Yet, it is clear that a scenario with small but nonzero determinant of the tensor A is numerically challenging and a more robust strategy is useful.

For this purpose, we note that the change of coordinates

$$T_B : S^2 \rightarrow S^2, \quad q \mapsto \frac{B^{-1/2} q}{\|B^{-1/2} q\|} \quad (2.25)$$

transforms the integral (2.24) into the form

$$\begin{aligned} & \frac{1}{4\pi} \int_{S^2} f(p) \left(p^T B p \right)^{-\frac{3}{2}} dS(p) \\ &= \frac{1}{4\pi} \int_{S^2} f(T_B(q)) dS(q), \end{aligned} \quad (2.26)$$

see Ospald et al. [72]. In particular, integrating against the ACG density (2.20) gets translated into an integration task for the uniform distribution on the unit sphere $S^2 \subseteq \mathbb{R}^3$. With this insight at hand, suppose a set $q_1, \dots, q_N \in S^2$ of integration points with corresponding positive weights w_1, \dots, w_N is given, which permits to approximate integrals of the form

$$\frac{1}{4\pi} \int_{S^2} g(q) dS(q) \approx \sum_{i=1}^N g(q_i) w_i. \quad (2.27)$$

Then, we may approximate the integral (2.26) by the expression

$$\begin{aligned} & \frac{1}{4\pi} \int_{S^2} f(p) \left(p^T B p \right)^{-\frac{3}{2}} dS(p) \\ & \approx \sum_{i=1}^N f(T_B(q_i)) w_i. \end{aligned} \quad (2.28)$$

Returning to our original task (2.22), we are thus left with solving the equation

$$\sum_{i=1}^N T_B(q_i) \otimes T_B(q_i) w_i \stackrel{!}{=} A \tag{2.29}$$

for B provided A is given. Still, the problem with the determinant remains. For this purpose, we record that the transformation (2.25) is invariant w.r.t. the scaling $B \mapsto \lambda B$ for any $\lambda > 0$. Moreover, computing the inverse square root of a matrix comes with a certain degree of computational effort. Therefore, we introduce the quantity $C = B^{-1/2} / \text{tr}(B^{-1/2})$, so that

$$T_B(q) \equiv \frac{B^{-1/2}q}{\|B^{-1/2}q\|} = \frac{Cq}{\|Cq\|} \tag{2.30}$$

holds. Whenever $\det C > 0$, the matrix B may be recovered. However, the matrix C also makes sense in the degenerate case. For instance, if all orientations are contained in the 1-2-plane, setting the $(i, 3)$ -components of the matrix B ($i = 1, 2, 3$) to zero projects all vectors q onto the 1-2-plane. Therefore, we are led to solving the equation

$$\sum_{i=1}^N p_i \otimes p_i w_i \stackrel{!}{=} A \quad \text{with} \quad p_i = \frac{Cq_i}{\|Cq_i\|} \tag{2.31}$$

for the symmetric matrix $C \in \mathbb{R}^{3 \times 3}$ with unit trace. As the matrices A and C share the same eigenbasis [64,65], it is numerically convenient to diagonalize the Eq. (2.31) with non-increasing diagonal elements in A and to eliminate the 33-component of the C -matrix explicitly

$$0 = \text{tr}(C) \quad \text{precisely if} \quad C_{33} = 1 - C_{11} - C_{22}. \tag{2.32}$$

Then, Eq. (2.31) becomes a nonlinear equation for only two variables, and conventional numerical root finding strategies may be applied.

To conclude this section, let us remark that we found using symmetric (antipodal) spherical t -designs [73] quite useful as general-purpose integration points with equal weights. Moreover, having the matrix B at our disposal is not necessary for the developments in this article. Rather, the matrix C is sufficient. For instance, the fourth-order fiber-orientation tensor \mathbb{A} may be computed as follows

$$\mathbb{A} = \sum_{i=1}^N p_i \otimes p_i \otimes p_i \otimes p_i w_i \quad \text{with} \quad p_i = \frac{Cq_i}{\|Cq_i\|}. \tag{2.33}$$

3 Computational methods

3.1 Efficient sampling from a Weibull distribution

Suppose a rectangular computational cell $Q = [0, Q_1] \times [0, Q_2] \times [0, Q_3]$ with positive edge lengths Q_i ($i = 1, 2, 3$) is given, together with a fiber-length distribution ρ , a fixed diameter d and a targeted fiber-volume fraction ϕ . We wish to sample a number N of cylindrical fibers with lengths ℓ_1, \dots, ℓ_N which follow the distribution ρ and realize the desired volume fraction ϕ as closely as possible, i.e., the condition

$$\frac{\pi d^2}{4Q_1 Q_2 Q_3} \sum_{i=1}^N \ell_i \stackrel{!}{\approx} \phi \tag{3.1}$$

should hold. If the fiber lengths are uniform, i.e., $\ell_i \equiv \bar{\ell}$ holds for all indices i , we may choose

$$N = \left\lceil \frac{4Q_1 Q_2 Q_3 \phi}{\pi d^2 \bar{\ell}} \right\rceil, \tag{3.2}$$

where the brackets denote rounding to the nearest integer. For a general fiber-length distribution, a similar approach could be pursued with the (number-weighted) mean

$$\mu = \int_0^\infty \ell \rho(\ell) d\ell \tag{3.3}$$

in place of the parameter $\bar{\ell}$ in Eq. (3.2). However, such an approach suffers from inaccuracies when computing the empirical number-weighted mean compared to the exact value. In particular, errors may be introduced compared to the desired volume fraction ϕ .

An alternative approach proceeds by sampling fiber lengths ℓ_1, ℓ_2, \dots inductively and to stop whenever the running sum

$$\frac{\pi d^2}{4Q_1 Q_2 Q_3} \sum_{i=1}^{\tilde{N}} \ell_i \tag{3.4}$$

exceeds the desired volume fraction ϕ . Then, the number of sampled fibers N is either chosen as \tilde{N} or $\tilde{N} - 1$, depending on which number leads to a closer agreement with the targeted fiber-volume fraction.

The simplest strategy proceeds by sampling the lengths in a *random* fashion from the given probability distribution ρ . However, a rather large number of samples is required to approximate the desired characteristics of the prescribed fiber-orientation distribution closely. Indeed, for any random variable $f : [0, \infty) \rightarrow \mathbb{R}$, the exact expectation

$$\int_0^\infty f(\ell) \rho(\ell) d\ell \tag{3.5}$$

is approximated by the empirical expectation

$$\frac{1}{N} \sum_{i=1}^N f(\ell_i). \tag{3.6}$$

For instance, in case $f(\ell) = \ell$, this difference concerns the (number-weighted) mean length, and similarly for the standard deviation. For a random variable with finite variance, random sampling leads to an error which decreases as $1/\sqrt{N}$. Put differently, to decrease the error by one order of magnitude, the sample size needs to be increased by a factor 100.

For the Weibull distribution (2.9), the integral (3.5) attains the specific form

$$\int_0^\infty f(\ell) \rho_{\lambda,k}(\ell) d\ell \equiv \int_0^\infty f(\ell) \frac{k}{\lambda} \left(\frac{\ell}{\lambda}\right)^{k-1} e^{-(\ell/\lambda)^k} d\ell, \tag{3.7}$$

which we may rewrite in the form

$$\begin{aligned} & \int_0^\infty f(\ell) \frac{k}{\lambda} \left(\frac{\ell}{\lambda}\right)^{k-1} e^{-(\ell/\lambda)^k} d\ell \\ &= \int_0^1 f\left(\lambda(-\ln u)^{1/k}\right) du \end{aligned} \tag{3.8}$$

with the substitution $u = e^{-(\ell/\lambda)^k}$. In particular, the transformation

$$T_{\lambda,k} : (0, 1) \rightarrow (0, \infty), \quad \lambda(-\ln u)^{1/k}, \tag{3.9}$$

permits us to push forward any sampling method on the unit interval to length space, giving rise to a sampling method for the Weibull distribution. Instead of the classical random sampling on the unit interval, which may be interpreted as a Monte Carlo integration rule [74], we rely on quasi-random sampling [75], which is based on low-discrepancy sequences [76]. Assuming sufficient smoothness of the integrand f , quasi-random sampling leads to an error which decreases as $1/N$ up to a logarithmic correction [76]. Roughly speaking, to reduce the error by an order of magnitude, the number of sampling points needs to be increased by a factor of ten. Further improvements may be reached by the scrambling technique [77], which gives rise to an error which decreases roughly as $1/N^{3/2}$, sufficient smoothness of the integrand premised.

Figure 3 shows a comparison for the different sampling methods. We consider random sampling, together with (scrambled and non-scrambled) Sobol sequences [78,79], implemented in PyTorch [80]. To get reproducible results, we ran the sampling 20 times and computed the average of the relative error. Moreover, we consider the Weibull data set

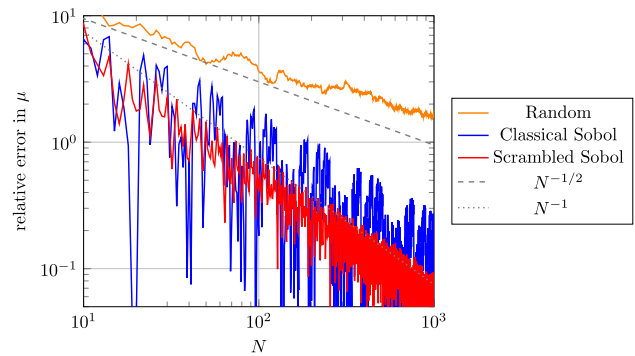


Fig. 3 Relative error of the empirical mean relative to the exact mean for different sampling strategies and with Weibull parameters $\lambda = 308.16\mu\text{m}$ and $k = 2.26$, see sect. 4.5, averaged over 20 sampling runs

to be inspected in Sect. 4.4, corresponding to actual fiber-length data from a μCT scan.

We observe that, for random sampling, the relative error converges only slowly, roughly at the predicted $N^{-1/2}$ rate. Even for $N = 1000$ samples, the relative error exceeds one percent. The Sobol sequence leads to a smaller error compared to random sampling for all sample sizes. There is a fluctuation by about an order of magnitude. Yet, even the worst-case is much better than random sampling, typically by roughly half an order of magnitude. For $N = 1000$ fibers, the relative error in the number-weighted mean is smaller than 0.5%. A relative error of 1% is already achieved at $N = 200$ samples in the worst-case scenario. Thus, only one fifth of the number of samples is necessary to reach the accuracy of the random sampling. Last but not least, we turn our attention to sampling based on scrambled Sobol sequences [77]. We observe an error scaling as N^{-1} , which is slightly than expected from theory. Still, the error scales roughly as for non-scrambled Sobol sampling, but at half a magnitude lower. In particular, for $N = 1000$ samples, the relative error is below 0.1%. In turn, 1% relative error is reached for as little as 80 samples. Please keep in mind that scrambled Sobol sequences involve a degree of randomness as well, enabling a statistical error estimation based on the empirical (unbiased) variance in a similar way as for purely random sampling. Thus, scrambled Sobol sequences represent the method of choice for our purposes, and are to a significant extent-responsible for the high degree of reproducibility of the results of the computations in Sect. 4.

3.2 Robust sampling from an ACG distribution

In this section, we discuss how to sample fibers when using the exact closure approximation [64,65]. This is possible, as the exact closure approximation comes with a full fiber-orientation density function

$$\varphi_B^{\text{ex}}(p) = \frac{1}{4\pi} \left(p^T B p \right)^{-\frac{3}{2}}, \quad p \in S^2, \tag{3.10}$$

the angular central Gaussian distribution [66]. Sampling from this distribution is straightforward. However, complications arise whenever the fiber orientation degrades to a two-dimensional state. Such a state cannot be described by a continuous distribution function, as a continuous function on the sphere, which vanishes everywhere except for a plane, has to vanish everywhere.

As a remedy, we re-use ideas from sect. 2.3. Recall that using a symmetric positive semidefinite matrix $C \in \mathbb{R}^{3 \times 3}$ with trace one turned out to be more convenient when describing the exact closure approximation encompassing the degenerate cases. Suppose the matrix C is identified as a solution of Eq. (2.31). Let ℓ_1, \dots, ℓ_N denote the fiber lengths drawn in the previous section. Then, we draw N vectors $q_i \in \mathbb{R}^3$ from a standard normal distribution in three dimensions in a random fashion. Finally, the transformation

$$p_i = \frac{C q_i}{\|C q_i\|}, \quad i = 1, \dots, N, \tag{3.11}$$

gives rise to appropriate directions for the fibers in an asymptotically consistent and robust way. Please note that we rely upon classical random sampling, as the eventual match of the realized fourth-order fiber-orientation tensor with the exact fourth-order fiber-orientation tensor will be ensured by the SAM method, to be described in the next section.

3.3 An augmented SAM algorithm

The sequential addition and migration (SAM) algorithm [25] is a method for generating periodic assemblings of non-overlapping cylindrical fibers with a prescribed volume fraction and fourth-order fiber-orientation tensor. Upon convergence, the algorithm produces a fiber structure which is perfectly periodic, where no pair of distinct fibers overlap and where both the desired volume fraction and the targeted fourth-order fiber-orientation tensor are realized up to the prescribed numerical precision. Originally, the method was introduced for fibers with an equal fiber length. In this work, we report on an extension of the methodology.

For a the cell $Q = [0, Q_1] \times [0, Q_2] \times [0, Q_3]$ and a given fourth-order fiber orientation tensor \mathbb{A} , for instance arising from a closure approximation, we suppose that the fiber lengths ℓ_1, \dots, ℓ_N and initial fiber orientations p_1^0, \dots, p_N^0 have been drawn in such a way that the target fiber-volume fraction is realized to the desired degree. Moreover, we initialize the fiber centers x_1^0, \dots, x_N^0 by drawing from a uniform distribution on the cube $[0, \max(Q_1, Q_2, Q_3)]^3$ and discarding those centers which lie outside of the cell Q . The

SAM algorithm [25] proceeds by the iterative scheme

$$\begin{aligned} x_i^{k+1} &= x_i^k + \tau \sum_{j=1}^N \delta_{ij}^k \frac{\xi_{ij}^k}{\|\xi_{ij}^k\|} \pmod{Q}, \\ p_i^{k+1} &= \begin{cases} p_i^k, & \|d_i^k\| = 0, \\ \cos(\|d_i^k\|) p_i^k + \sin(\|d_i^k\|) d_i^k / \|d_i^k\|, & \text{otherwise,} \end{cases} \end{aligned} \tag{3.12}$$

for $i = 1, \dots, N$ and a step size τ , typically chosen as 0.3. Here, the vector ξ_{ij}^k realizes the distance between the spheroids described by the triples (x_i^k, p_i^k, ℓ_i) and (x_j^k, p_j^k, ℓ_j) , and $\delta_{ij}^k = \max(0, D - \|\xi_{ij}^k\|)$ in terms of the fiber diameter D . The vector d_i^k computes as

$$\begin{aligned} d_i^k &= (\text{Id} - p_i^k \otimes p_i^k) \left[\frac{\ell_i}{n_i} \sum_{j=1}^N \delta_{ij}^k \frac{s_{ij}^k}{2} \frac{\xi_{ij}^k}{\|\xi_{ij}^k\|} + (\mathbb{A} - \mathbb{A}^k) \dots \right. \\ &\quad \left. p_i^k \otimes p_i^k \otimes p_i^k \right] \end{aligned} \tag{3.13}$$

with the parameter

$$\varepsilon_i = \frac{D^2}{\frac{2}{3} + a_i} \left(\frac{a_i^3}{12} + \frac{a_i^2}{6} + \frac{3a_i}{16} + \frac{1}{15} \right), \quad a_i = \ell_i/D, \tag{3.14}$$

the current orientation tensor

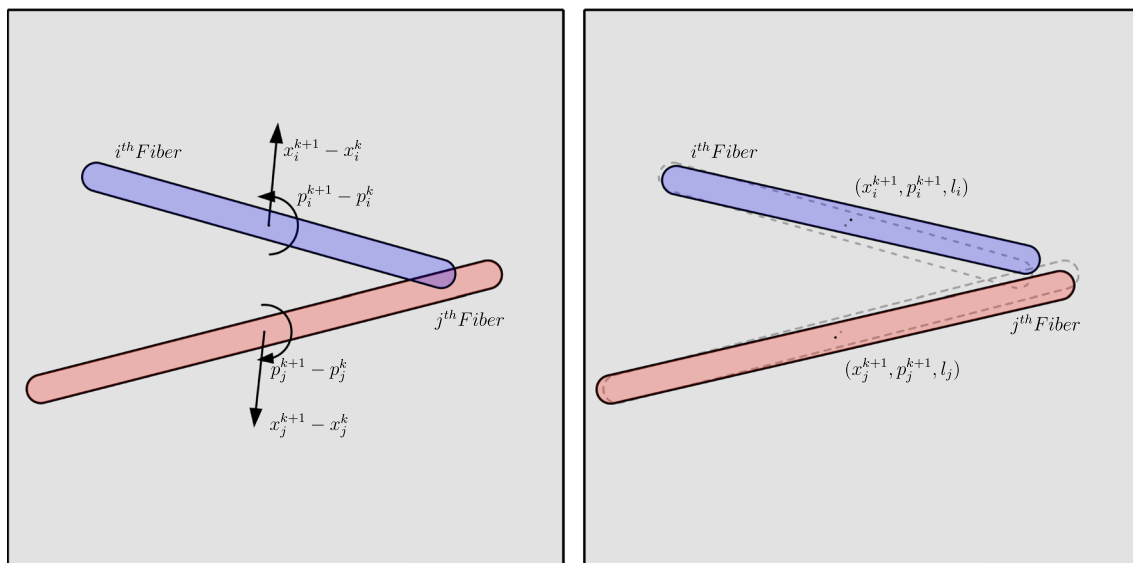
$$\mathbb{A}^k = \sum_{i=1}^N \ell_i p_i^k \otimes p_i^k \otimes p_i^k \otimes p_i^k / \sum_{i=1}^N \ell_i \tag{3.15}$$

and $s_{ij}^k \in [-1, 1]$ defined by equation (4) in Schneider [25].

To illustrate the procedure, let us investigate what happens when two fibers do intersect, as shown in Fig. 4a. In order to remove the overlap, the fibers have the option to move their centers x_i and x_j , respectively, or to rotate their directions p_i and p_j appropriately. The distance to move is governed by the overlap parameter δ_{ij} , and encoded by formula (3.12). Of course, it is necessary to balance the shifts of the centers and the rotations appropriately, see Fig. 4b. This is done implicitly via the parameter n_i in (3.3) that arises from the inertia tensor of the corresponding spherocylinder.

The iterative scheme (3.12) is terminated whenever the fibers are in a non-overlapping condition and the match between the fourth-order fiber-orientation tensors is sufficiently good. We use a relative difference in Frobenius norm of the Voigt representations of the tensors below 10^{-4} for this article throughout.

The bulk of the computational effort of the SAM algorithm (3.12) is hidden in determining the inter-particle collisions. Indeed, for N fibers, a naive implementation requires $N(N +$



(a) A pair of overlapping fibers with different length

(b) Updated fiber configuration after a step (3.12)

Fig. 4 Illustration of the update formula (3.12) for two individual fibers

1)/2 overlap checks. To reduce this effort, we utilize nested Verlet lists as proposed in Schneider [25].

When it comes to a fiber-length distribution, an additional difficulty arises. In the original work [25], fibers were assumed to be shorter than half the cell dimensions. In this way, periodic distance computations could be carried out with minimum effort. However, when considering a distribution of the fiber length it is rather typical that there are a few rather long fibers. If the cell dimensions were required to exceed the maximum length by a factor of two, the considered cells would be rather large. Thus, a workaround is required.

Suppose we wish to compute the distance between two fibers (x_i, p_i, ℓ_i) and (x_j, p_j, ℓ_j) on a periodic cell $Q = [0, Q_1] \times [0, Q_2] \times [0, Q_3]$. Suppose that the fiber length ℓ_i exceeds $Q/2$ for $Q = \min(Q_1, Q_2, Q_3)$. Then, we break the first fiber into K individual segments, each of which is shorter than $Q/2$, and compute the K distances between the fiber segments and the j -th fiber. This strategy is illustrated in Fig. 5a, where the red fiber is decomposed into $K = 7$ segments. The shortest distance among these computed distances is then selected as the distance between the entire i -th fiber and the j -th fiber. Clearly, if the j -th fiber exceeds the length requirements, a similar approach is successful.

Last but not least let us mention the possibility that a rather long fiber intersects itself. Such a situation may be handled by a modification of the proposed strategy. The fiber is broken into K segments. Then, overlap is checked between the non-adjacent segments. This is illustrated in Fig. 5b for a fiber that is decomposed into $K = 5$ segments. Only between the pairs with a \surd sign, an overlap check needs to be made. Due

to symmetry, six checks need to be made for the example at hand. In case of overlap, an additional term (for $i = j$) arises in the sums (3.12) and (3.13).

4 Computational investigations

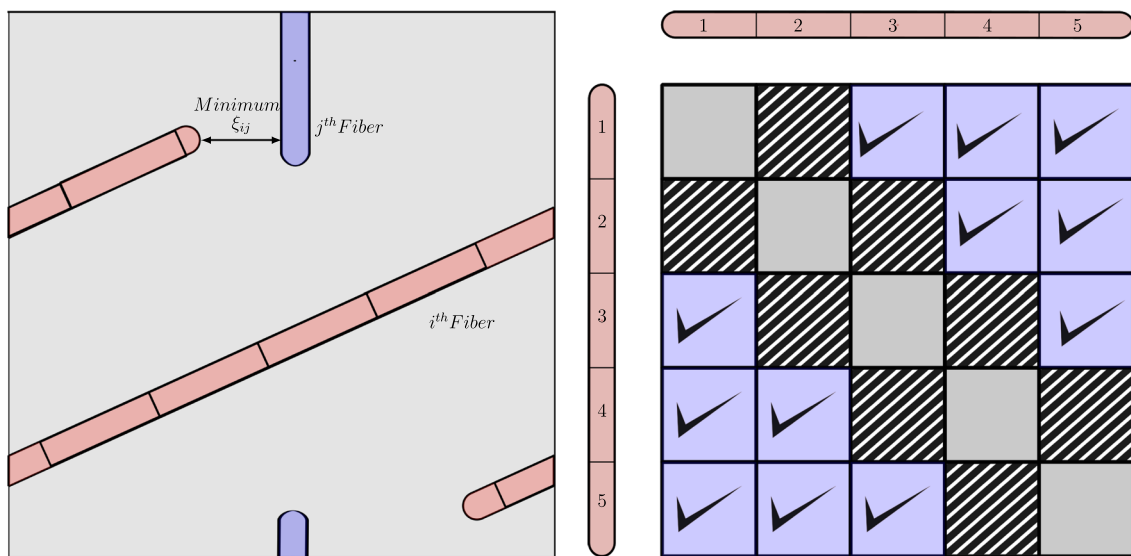
4.1 Setup

The presented algorithms were implemented in Python with Cython extensions. Most of the code runs in serial, only the inter-fiber distance computations were parallelized with OpenMP. The timings were recorded on a PC with a six-core Intel i7 CPU and 32GB RAM.

For computing the effective elastic properties, we rely upon an FFT-based computational homogenization code [81,82]. We utilize a discretization on a staggered grid [83], which is solved by a conjugate gradient method [84–86] up to a relative tolerance of 10^{-5} . We refer to the overview article [87] for background.

To compute the effective elastic constants, we compute the effective stresses corresponding to six independent strain loadings. Subsequently, the effective elasticity tensor is approximated by an orthotropic fourth-order tensor [88] to enable interpreting the corresponding engineering constants.

As our point of departure, we consider a commercially available PA6GF35, i.e., a polyamide-6 matrix with 35% (by weight) glass-fiber reinforcement. As our “standard setup” we select fibers with a diameter of $10\mu\text{m}$ and a length of $250\mu\text{m}$. The data is summarized in Table 2. The matrix and fiber are furnished with the isotropic elastic parameters given in Table 1, following Hessman et al. [40].



(a) Decomposing a rather long fiber (i) to check intersection with the blue fiber (j) (b) Necessary checks between sub-segments for a self-intersection check of a long fiber with $K = 5$ segments

Fig. 5 Illustrating the decomposition approach of fibers to handle both fiber-fiber overlap checks and self-intersection

4.2 On the necessary resolution

To compute the effective mechanical properties of composites, a number of error sources needs to be quantified. The most obvious such error source is the resolution, i.e., the mesh size of the discretization. Under appropriate hypotheses, the effective properties converge upon mesh refinement [89–91]. In particular, a sufficiently fine mesh is mandatory for accurate results. On the other hand, fine meshes also come with a higher number of degrees of freedom, increasing the computational effort significantly. Indeed, for regular meshes in three spatial dimensions, the effort of FFT-based solution techniques were shown to roughly increase by a factor of eight when halving the mesh width [83,86], which is close to optimal for these kinds of problems. Therefore, a suitable

Table 1 Model parameters adjusted to experimental data [40]

Material	E in GPa	ν
E-glass fibers	72.0	0.22
PA6 matrix	3.0	0.4

Table 2 Typical properties of the unit cells, serving as point of departure

Fiber volume fraction	19.3%
Closure approximation	Exact, Eq. (2.20)
Fiber length	$250\mu\text{m}$
Fiber diameter	$10\mu\text{m}$

compromise between accuracy and manageable computational effort needs to be chosen.

We consider the setup shown in Table 2, in particular with a uniform fiber length. Such an approach eliminates other sources of error, e.g., coming from the fiber-length distribution. We generated cubic microstructures with an edge length of $300\mu\text{m}$, one for the three second-order fiber-orientation tensors

$$\begin{aligned}
 A^{\text{iso}} &= \text{diag}(1/3, 1/3, 1/3), \\
 A^{\text{piso}} &= \text{diag}(1/2, 1/2, 0) \quad \text{and} \\
 A^{\text{ud}} &= \text{diag}(1, 0, 0),
 \end{aligned}
 \tag{4.1}$$

corresponding to isotropic, planar isotropic and unidirectional (i.e., aligned) fiber-orientation states.

We set the isolation distance between fibers to $2\mu\text{m}$, i.e., 20% of the fiber diameter consistently throughout the manuscript.

We change the resolution by considering different voxel sizes $4\mu\text{m}$, $2\mu\text{m}$, $1\mu\text{m}$ and $0.5\mu\text{m}$, giving rise to voxel models with 75^3 , 150^3 , 300^3 and 600^3 hexahedron elements, see Fig. 6 for an illustration in the case of an isotropic fiber orientation. For the finest resolution, a single fiber is resolved by 20 voxels across the diameter. This resolution decreases to ten and five voxels per diameter for a voxel size of $1\mu\text{m}$ and $2\mu\text{m}$. The coarsest resolution, $h = 4\mu\text{m}$, works with only 2.5 elements per fiber diameter, on average.

The effective directional Young’s moduli of the orthotropic approximation of the effective elastic properties are shown in Fig. 7 for the three considered fiber-orientation states (4.1). For the isotropic orientation, we observe that the three direc-

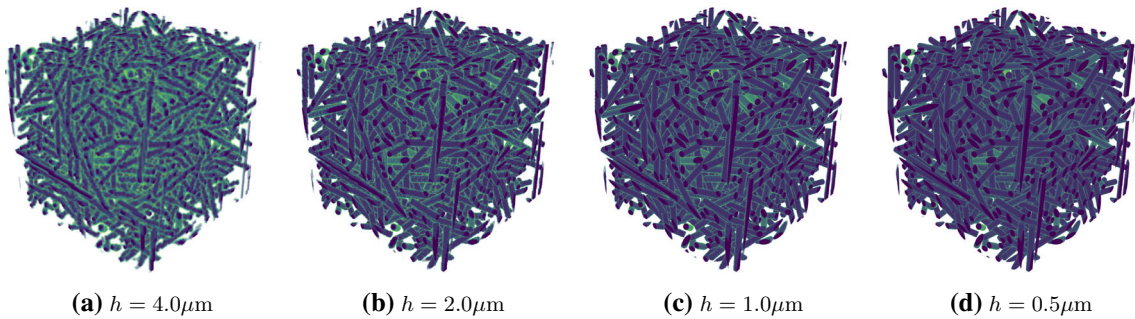
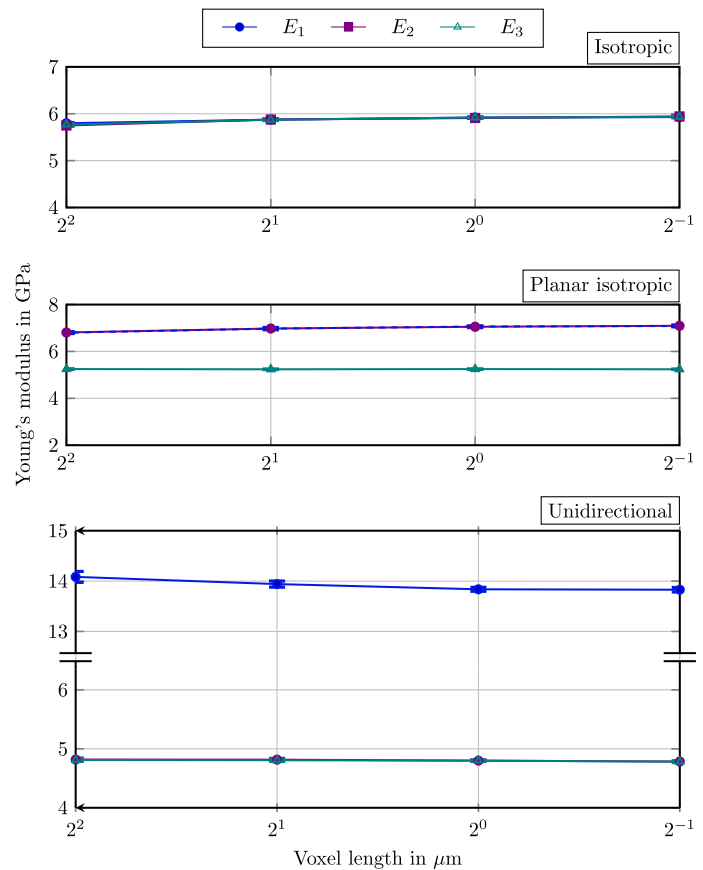


Fig. 6 Illustration of a $(300\mu\text{m})^3$ -microstructure with isotropic fiber orientation, resolved with different voxel edge-lengths h

Fig. 7 Influence of the voxel edge-length h on the effective directional Young's moduli



tional Young's moduli are almost identical for all resolutions considered, conforming to our expectations. Decreasing the resolution also decreases the effective Young's modulus. For $h = 4\mu\text{m}$, the effective Young's modulus E_1 differs by 4.36% from the highest resolution. This deviation decreases to 0.9% and 0.2% for $h = 2\mu\text{m}$ and $h = 1\mu\text{m}$, respectively. For the other two Young's moduli, the deviations are rather similar.

For the planar isotropic case, the in-plane Young's moduli E_1 and E_2 exceed the out-of-plane Young's modulus E_3 . Coarsening the resolution has little influence on E_3 . Even the coarsest resolution deviates only by 1.3% from the finest

resolution. For the Young's moduli E_1 and E_2 , such a coarsening leads to a slight underestimation of the moduli. For the coarsest resolution, there is an 6.6% deviation in E_1 . For $h = 2\mu\text{m}$ and $h = 1\mu\text{m}$, the relative deviations decrease to 1.6% and 0.3%, respectively. For E_2 , the relative errors are similar. For the out-of-plane modulus E_3 , the relative deviation to the finest resolution is at 1.3%. Refining the resolution leads to even lower errors, at 0.01% and 0.15%.

For the uni-directional case, the transverse Young's moduli E_2 and E_3 coincide to the naked eye. They are much smaller, almost by a factor of three, than the parallel Young's modulus E_1 . At the coarsest resolution, E_2 is already 0.3%-

close to the value at the highest resolution. Similarly, the coarsest resolution overestimates the modulus E_1 1.1%.

To sum up, we observe that the largest errors occur for the planar isotropic fiber orientation, and for the in-plane Young's moduli. Selecting $h = 2\ \mu\text{m}$ ensures that the Young's moduli are computed with less than 2% relative error, giving us sufficient confidence in the obtained results.

4.3 On the size of the representative volume element

Due to the randomness of the geometry of fiber-reinforced composites, the computed apparent elastic properties on unit cells involve a degree of randomness, as well. The effective properties, which are deterministic, emerge only upon considering sufficiently large cells, so-called representative volume elements [26–28]. A large body of studies were devoted to this concept (see Doškář et al. [92] for a recent overview), in particular as an increased size of the considered volume element necessarily increases the computational effort, as well. Therefore, it is desirable to work with volume elements that are large enough to closely approximate the effective properties and, at the same time, as small as possible to keep the effort manageable.

The errors emerging when working with finite-sized cells may be naturally classified into two categories. Suppose we work with a cubic cell with an edge length \underline{Q} . In this section, we write \underline{Q} to emphasize that we work with a cubic cell. The apparent elastic properties computed for cells of this size fluctuate around a mean, and the associated variance quantifies the stochastic fluctuations of the elastic properties. This so-called random error (or dispersion) depends on the cell size and becomes smaller as the cell edge-length \underline{Q} increases, with a rate that depends on the underlying stochastic model for the microstructure [28,93,94]. In addition to the random error, there might be a difference between the mean properties computed for a fixed cell size and the effective properties [28,95]. This error is called systematic error (or bias), and is more difficult to assess and grasp. Typically, the random error is much larger than the systematic error, and the attention focuses on a suitable estimation of the random error.

Previous studies have shown that both the random and the systematic error increase when using traction or displacement boundary conditions or working with non-periodized geometries [28,96,97]. As our generated microstructures are intrinsically periodic, the periodic boundary conditions that come naturally with FFT-based solvers do help us in this regard.

We would like to understand whether increasing the variance in the fiber length also necessitates working with larger unit cells. For this purpose, we consider a uniform fiber-length distribution as our point of departure.

We investigate the three extreme fiber-orientation states (4.1) with the setup described in Table 2, the material parameters of Table 1 and the previously identified voxel size $h = 2\ \mu\text{m}$. We consider three cubic unit-cell sizes, with edge lengths $\underline{Q} = 300\ \mu\text{m}$, $\underline{Q} = 600\ \mu\text{m}$ and $\underline{Q} = 900\ \mu\text{m}$. The smallest edge length, $\underline{Q} = 300\ \mu\text{m}$, only slightly exceeds the fiber length $\bar{\ell} = 250\ \mu\text{m}$.

The results of ten runs are recorded in Fig. 3. The orthotropic approximation error lies around 1%, and is thus smaller than the error induced from the resolution. In particular, it is meaningful to only consider the orthotropic engineering constants. We observe that the standard deviations of the directional Young's moduli are on a rather small level—they do not exceed 0.5% of the corresponding mean for $\underline{Q} = 300\ \mu\text{m}$. Increasing the cell size decreases the standard deviation, as well. For $\underline{Q} = 600\ \mu\text{m}$, the standard deviations do not exceed 0.2%, and drop to less than 0.09% for $\underline{Q} = 900\ \mu\text{m}$.

Concerning the systematic error, the highest deviation is reached for E_1 in the unidirectional case with a relative deviation of 1.2% compared to the large-scale modulus.

With these reference results at hand, we consider a Weibull-distributed fiber-length distribution with a (volume-weighted) mean fiber length $m = 250\ \mu\text{m}$ and a standard deviation $s = 100\ \mu\text{m}$, see also Fig. 2 for an illustration of the fiber-length distribution function. The statistical measure of ten runs are collected in Table 4. Further complications arose for the unidirectional case and the smallest considered edge length $\underline{Q} = 300\ \mu\text{m}$. If a fiber of length ℓ is axis-aligned in a cubic cell with edge length \underline{Q} , it will always intersect itself if $\ell \geq \underline{Q}$, i.e., if the fiber length is larger or equal to the cell edge-length. For the considered standard deviation, a non-trivial number of fibers were simply too long to fit into the cell with $\underline{Q} = 300\ \mu\text{m}$. Therefore, after drawing the fiber length ℓ , we restricted it as follows

$$\ell \leftarrow \min(\ell, 0.99 \underline{Q}). \quad (4.2)$$

For non-UD fiber orientations, this issue did not arise.

Taking a look at the results collected in Table 4, we observe that the mean values do in fact differ from the reference results with zero variance, but the standard deviations of the apparent Young's moduli are on a similar level. Indeed, Fig. 8 compares the relative standard deviations of the considered orthotropic Young's moduli for the investigated orientations and varying cell edge-length. The standard deviations do not exceed 0.5% for the smallest cells, and decreases for increasing cell size. For $\underline{Q} = 300\ \mu\text{m}$, the standard deviations are a bit larger than for $s = 0$, but not significantly so. Similarly, the systematic error is also on a rather low level. Indeed, even for E_1 in the aligned case, the relative deviation between the means of the smallest and the largest cell is as low as 1.6%, even for the cropped fiber lengths (4.2).

Table 3 Orthotropic Young's moduli (mean \pm standard deviation for ten runs) for RVE study with uniform fiber length $\bar{\ell} = 250 \mu\text{m}$

orientation	\underline{Q} in μm	E_1 in GPa	E_2 in GPa	E_3 in GPa	err_{orth} in %
iso	300	5.875 ± 0.011	5.875 ± 0.014	5.868 ± 0.013	1.041 ± 0.061
	600	5.868 ± 0.005	5.868 ± 0.005	5.868 ± 0.003	1.057 ± 0.018
	900	5.867 ± 0.003	5.867 ± 0.003	5.869 ± 0.002	1.060 ± 0.015
piso	300	6.947 ± 0.029	5.526 ± 0.014	5.529 ± 0.011	1.052 ± 0.048
	600	6.925 ± 0.008	5.521 ± 0.002	5.520 ± 0.003	1.022 ± 0.011
	900	6.921 ± 0.006	5.518 ± 0.002	5.518 ± 0.002	1.014 ± 0.004
ud	300	14.030 ± 0.065	4.816 ± 0.023	4.811 ± 0.023	0.594 ± 0.048
	600	13.861 ± 0.025	4.814 ± 0.003	4.813 ± 0.006	0.589 ± 0.014
	900	13.834 ± 0.011	4.812 ± 0.003	4.813 ± 0.003	0.584 ± 0.006

Table 4 Orthotropic Young's moduli (mean \pm standard deviation for ten runs) for RVE study with (volume-weighted) mean fiber length $m = 250 \mu\text{m}$ and standard deviation $s = 100 \mu\text{m}$

orientation	\underline{Q} in μm	E_1 in GPa	E_2 in GPa	E_3 in GPa	err_{orth} in %
iso	300	5.813 ± 0.022	5.821 ± 0.019	5.818 ± 0.015	1.021 ± 0.046
	600	5.801 ± 0.013	5.801 ± 0.008	5.797 ± 0.009	1.053 ± 0.028
	900	5.799 ± 0.004	5.798 ± 0.003	5.801 ± 0.004	1.039 ± 0.017
piso	300	6.864 ± 0.025	5.478 ± 0.025	5.477 ± 0.020	0.967 ± 0.081
	600	6.818 ± 0.014	5.465 ± 0.006	5.462 ± 0.008	0.998 ± 0.029
	900	6.819 ± 0.006	5.464 ± 0.004	5.465 ± 0.003	0.997 ± 0.010
ud	300	13.635 ± 0.030	4.819 ± 0.020	4.815 ± 0.022	0.604 ± 0.037
	600	13.414 ± 0.024	4.812 ± 0.004	4.811 ± 0.003	0.592 ± 0.008
	900	13.413 ± 0.019	4.811 ± 0.003	4.809 ± 0.004	0.592 ± 0.006

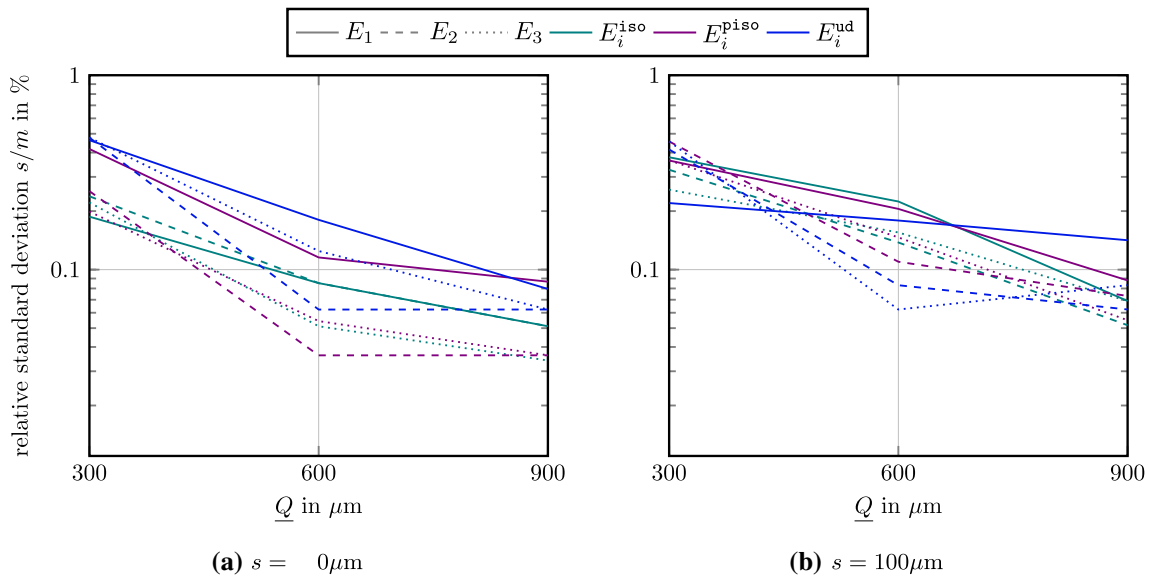


Fig. 8 Relative standard deviation of directional Young's moduli for increasing cubic edge length \underline{Q} , mean fiber length $m = 250 \mu\text{m}$ and two different standard deviations s

To sum up, we could show that working with a considerable fiber-length variability in the fiber-length distribution does not negatively affect the necessary cell size when computing the effective elastic properties of short-fiber composites.

4.4 Results of varying fiber-length parameters

In this section, we investigate the effects of varying the parameters of the Weibull fiber-length distribution. For this purpose, we continue to investigate the commercial PA6GF35 with parameters summarized in Table 1 and Table 2. To keep the number of changing parameters manageable, we restrict to a fixed fiber-orientation state, described by the exact closure of the second-order fiber-orientation tensor

$$A = \text{diag}(0.7855, 0.1962, 0.0183), \quad (4.3)$$

as determined by Hessman et al. [40] with a μ CT-based algorithm which identifies individual fibers [35]. Fig. 9 shows the influence of a change in the fiber-length distribution on the computed effective orthotropic Young's moduli of the composite. We consider variations of the (volume-weighted) mean and standard deviation individually. These changes correspond to the fiber-length distribution functions shown in Fig. 2. We start with a fixed standard deviation $s = 120 \mu\text{m}$ and a continuously changing standard deviation, see Fig. 9a and 9b. We observe that the transverse Young's moduli E_2 and E_3 are scarcely affected by such a change. In contrast, the longitudinal Young's modulus E_1 increases with increasing mean fiber length. Between $m = 250 \mu\text{m}$ and $m = 325 \mu\text{m}$, the modulus E_1 increases by roughly half a GPa. This difference increases even more when approaching the highly aligned case, e.g., unidirectional fibers.

Taking a look at varying standard deviations with fixed mean length $m = 250 \mu\text{m}$, see Fig. 9b, we also observe that the transverse Young's moduli are hardly affected. The longitudinal Young's modulus E_1 decreases with increasing standard deviation. This result conforms with mechanical intuition. It is not clear whether a saturation point is reached for $a \rightarrow \infty$, as generating the high standard deviations also came with the challenge of dealing with very long fibers (and exceedingly large volume elements). Moreover, for high standard deviation, the "turning point" is reached where the fiber-length distribution does not have a unique maximum any more, but shows a consistently decreasing trend. Yet, we observe a difference of roughly one GPa, i.e., about ten %, between a state with uniform fiber lengths and a strongly dispersed fiber-length distribution.

Last but not least, we investigate the runtime of the fiber-generation process, and how it is influenced by the fiber-length parameters.

Considering the three extreme orientations 4.1, we ran ten simulations on cubic volume elements with edge length

$\underline{Q} = 600 \mu\text{m}$. For a start, we consider a PA6GF35 with fixed standard deviation $s = 120 \mu\text{m}$ and increasing mean length m . The results are shown in Fig. 10a. The runtime for the unidirectional case is extremely small, as expected. Indeed, even random sequential addition (RSA) methods [14–17] are able to generate unidirectional states at high filler fraction. Non-aligned fiber-orientation states are more difficult to handle, and this is where most traditional algorithms have their limitations. Both for the isotropic and the planar isotropic fiber-orientation state, the overall runtimes never exceeded one minute. Taking into account the runtime of the subsequent computational homogenization, such an effort is clearly acceptable. We observe that, for almost all considered cases, generating the isotropic state required a higher effort than for the planar isotropic state. Moreover, increasing the mean fiber length also led to an increase in the runtimes for the isotropic case. The runtimes for the planar isotropic case were not adversely affected for increasing mean fiber length. Rather surprisingly, the runtime increased for the smallest considered fiber length. This behavior is rooted in the difficulty inherent to generating exactly planar fiber-orientation states. The problem comes from the fact that for a smaller mean fiber length, the number of considered fibers increases. In turn, attaining a purely planar fiber-orientation state becomes more difficult, i.e., the iteration count increases superlinearly with the fiber count.

To demonstrate the capabilities of the algorithm, we fixed the mean length as well as the standard deviation and increased the considered volume fraction. The results, see Fig. 10b, show that the algorithm was able to generate up to 30% filler fraction in less than three minutes in a reliable and robust manner. For the non-aligned orientations, we observe a strong increase in the runtimes necessary to generate the volume elements for increasing volume fraction.

4.5 Comparison to experimental data

In this section, we compare the introduced methodology to real data, both in terms of measured fiber-length data and concerning measured directional Young's moduli. Hessman et al. [40] consider a PA6GF35 with short-fiber reinforcement. Based on μ CT-scans, individual fibers were identified, permitting a subsequent statistical analysis. The fiber diameter emerged as $10 \mu\text{m}$, as expected, and the determined fiber-length distribution is shown in Fig. 11a. Moreover, the fiber-orientation tensors (2.4) may be determined, as well. The complete volume-averaged second-order fiber-orientation tensor is given in Eq. (4.3). However, an analysis of the fiber orientation across the thickness of the plate was also given [40, Fig. 4]. The orientation follows the classical skin-core-skin layering typical for short-fiber composites [98].

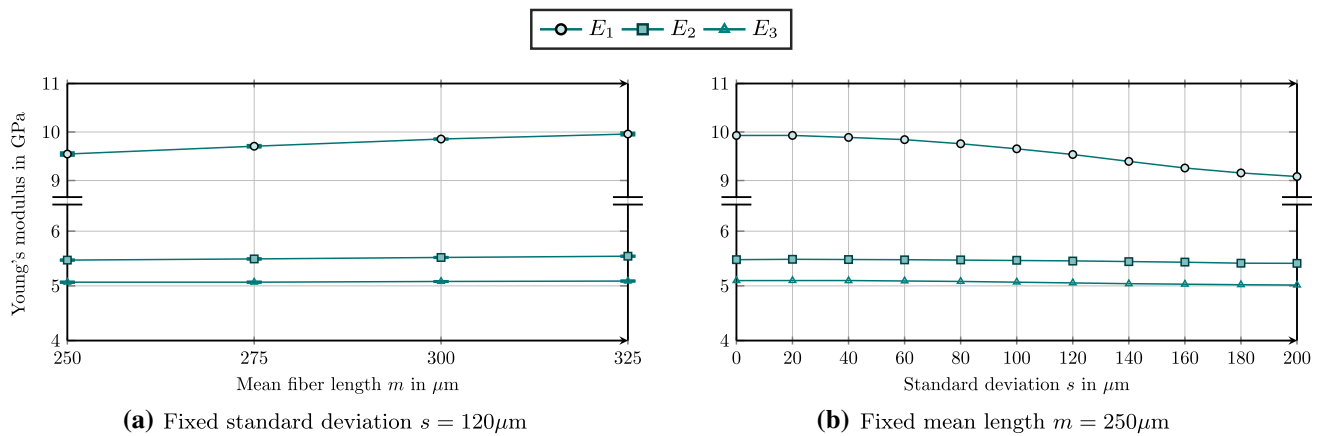


Fig. 9 Effect of varying (volume-weighted) mean fiber length and standard deviation for PA6GF35

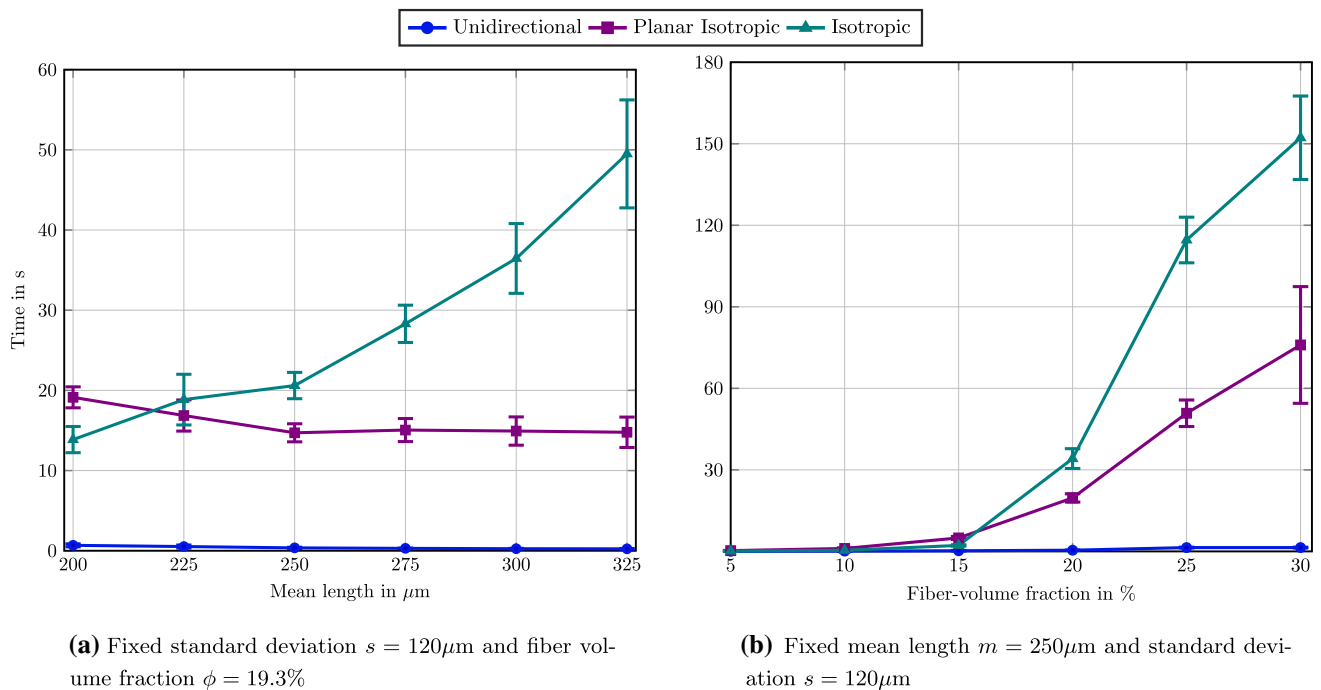


Fig. 10 Time to generate cubic volume elements with an edge length of $600 \mu\text{m}$

For a start, we fit the fiber-length data with a Weibull distribution, essentially by hand. The overall fit, see Fig. 11a, is rather accurate. The Weibull parameters

$$k = 2.26 \quad \text{and} \quad \lambda = 308.16 \mu\text{m} \quad (4.4)$$

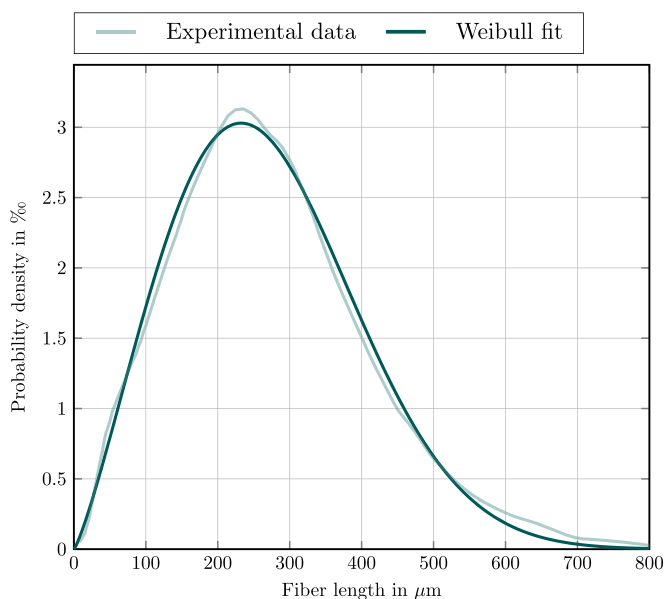
correspond to a (volume weighted) mean $m = 332.65 \mu\text{m}$ and a standard deviation $s = 127.64 \mu\text{m}$. With the identified Weibull distribution at hand, we generated suitable sandwich structures with $\underline{Q} = 800 \mu\text{m}$, see Fig. 11b, where the top and the bottom layer have a second-order fiber-orientation tensor

$$A^{\text{skin}} = \text{diag}(0.8602, 0.1227, 0.0171), \quad (4.5)$$

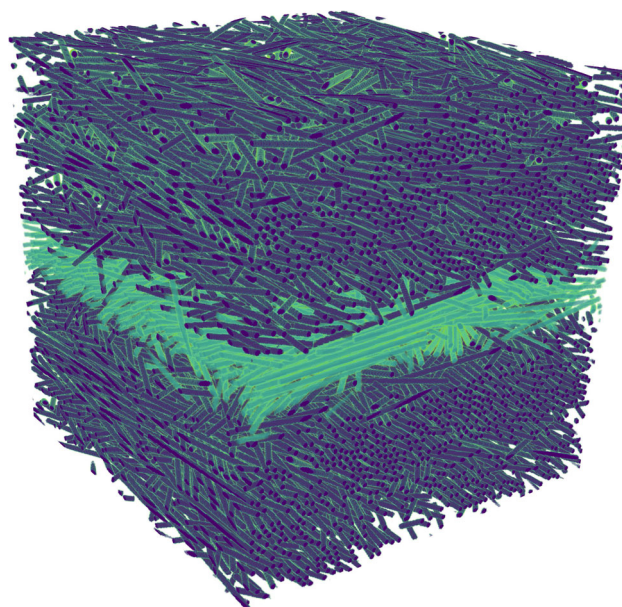
whereas the central layer, about 1/6th of the height, is characterized by

$$A^{\text{core}} = \text{diag}(0.2255, 0.7424, 0.0321), \quad (4.6)$$

augmented by the exact closure. The computed effective Young's moduli are recorded in Table 5. Compared to the experimental data, the longitudinal Young's modulus is reproduced with high accuracy. The transverse Young's modulus is slightly overestimated, but still contained in the 99.9%-confidence interval. We ran the simulations ten times, but the standard deviation of the effective moduli turned out to be negligible, again.



(a) Comparison of fiber-length data [40, Fig. 5] and a Weibull fit



(b) Exemplary sandwich microstructure

Fig. 11 Probability distribution and generated microstructure with layers following the study of Hessman et al. [35]

Table 5 Comparison of experimentally determined Young’s moduli ± standard deviation [40] and computed results, including runtimes, with different setups

	Experiments	Sandwich [40, Fig. 2]	Mean data	Fixed length
E_1 in GPa	10.34 ± 0.4	10.42 ± 0.03	9.91 ± 0.03	10.14 ± 0.01
E_2 in GPa	5.50 ± 0.1	5.78 ± 0.00	5.56 ± 0.02	5.54 ± 0.00
runtime in s	–	69.00 ± 8.45	71.75 ± 19.0	14.98 ± 3.42

As a comparison to the three-layered structure, we generated a volume element with a homogeneous fiber-orientation distribution (4.3) and the identified Weibull distribution, see Fig. 11a. The results, see *mean data* in Table 5, show that the longitudinal Young’s modulus is about half a GPa lower than for the sandwich structure. Also, the transverse Young’s modulus is about 0.2GPa lower. These results indicate that the load-carrying capacity of the layered structure is improved in both directions compared to the one without layers. Moreover, the longitudinal Young’s modulus lies below the experimental values, actually at the lower end of the confidence interval, whereas the transverse Young’s modulus matched quite well with the experimental value. Last but not least, we consider the case with only a single fiber length, fixed at $\bar{\ell} = m \equiv 332.65\mu\text{m}$. This case, labeled by *fixed length* in Table 5 leads to a slightly higher longitudinal Young’s modulus, which lies below both the experimental mean and the prediction for the sandwich structure. The transverse Young’s modulus is rather close to the *mean data* case, as was already observed in the previous section.

Last but not least, a glance at the runtime reveals that the runtime for the microstructure generation was significantly less than two minutes, for all cases considered.

5 Conclusion

This work was devoted to extending the SAM algorithm to varying fiber lengths and to studying the effects on the effective elastic properties of short-fiber reinforced plastics. We draw the following conclusions.

- There are many moments of the fiber length-orientation distribution (2.1)

$$M_{m,k} = \int_0^\infty \int_{S^2} \ell^m p^{\otimes k} \psi \, dS \, d\ell, \tag{5.1}$$

parametrized by non-negative integers m and k , which could be enforced in the SAM algorithm. For the work at hand, we considered $m = 1$ and $k = 4$, together with approximations for $M_{m,0}$ via the quasi-random sam-

pling of the fiber lengths. Such a strategy turned out to be successful in reducing the statistical variations of the computed effective elastic properties to a minimum. However, it might be of interest whether enforcing higher-order moments is beneficial for the effective of nonlinear and inelastic mechanical properties.

- We considered the Weibull distribution to describe the fiber-length distribution. Working with other fiber distributions is possible with little adaptation. For instance, long-fiber composites may show two distinct maxima in the fiber-length distribution function, as a result of fibers breaking during the manufacturing process.
- Our studies revealed that an increase in the standard deviation of the fiber length did not adversely affect the necessary RVE size. Such a result is encouraging, and should not be taken for granted. Indeed, a claim that an increase in the standard deviation would necessitate larger computational cells appears to be plausible. Yet, the influence of the fiber-length distribution appears to be more pronounced for inelastic material behavior, a topic which may deserve further studies.
- It was possible to closely match the longitudinal Young's modulus of the experimental structure, whereas the transverse Young's modulus was overestimated a little. There is a number of possible error sources. For a start, as only 80% of the individual fibers get segmented correctly, there is still some uncertainty in both the fiber orientation and the fiber-length distribution. Moreover, we do not have access to the layer-wise fourth-order orientation tensors whose consideration may certainly enhance the predictive quality. Last but not least, we consider the fiber-length distribution to be uniform throughout the thickness. Still, despite all these uncertainties, the match is certainly sufficient for most engineering applications.
- In this work, we relied upon the hypothesis that the fiber length and the fiber orientation are independent. Experimental data suggests otherwise, and the introduced error remains to be quantified. As a first step, it appears promising to estimate the entire fiber length-orientation distribution from the available data.
- We could show the benefits of the quasi-random sampling of the fiber length. This is a key technology, and we advocate it to become the standard for expressive fiber-generation tools. Moreover, the developed technology may also be used for long and flexible fibers.

Acknowledgements Support by the Deutsche Forschungsgemeinschaft (DFG, German Research Foundation)-projects 255730231 and 440998847- is gratefully acknowledged.

Funding Open Access funding enabled and organized by Projekt DEAL.

Open Access This article is licensed under a Creative Commons Attribution 4.0 International License, which permits use, sharing, adaptation, distribution and reproduction in any medium or format, as long as you give appropriate credit to the original author(s) and the source, provide a link to the Creative Commons licence, and indicate if changes were made. The images or other third party material in this article are included in the article's Creative Commons licence, unless indicated otherwise in a credit line to the material. If material is not included in the article's Creative Commons licence and your intended use is not permitted by statutory regulation or exceeds the permitted use, you will need to obtain permission directly from the copyright holder. To view a copy of this licence, visit <http://creativecommons.org/licenses/by/4.0/>.

Appendix A Weibull parameters from volume-weighted mean and variance

The purpose of this section is to derive the expressions (2.12) and (2.14) for the parameters λ and k of the Weibull distribution (2.9)

$$\rho_{\lambda,k}(\ell) = \frac{k}{\lambda} \left(\frac{\ell}{\lambda}\right)^{k-1} e^{-(\ell/\lambda)^k}, \quad \ell > 0, \quad (\text{A.1})$$

for prescribed volume-weighted mean m and standard deviation s , given by the formula

$$m = \frac{\langle \ell^2 \rangle}{\langle \ell \rangle} \quad \text{and} \quad s^2 = \frac{\langle (\ell - m)^2 \ell \rangle}{\langle \ell \rangle}, \quad (\text{A.2})$$

where we use the shorthand notation

$$\langle g \rangle = \int_0^\infty g(\ell) \rho_{\lambda,k}(\ell) d\ell \quad (\text{A.3})$$

for the (number-weighted) mean of any random variable g w.r.t. the Weibull distribution (A.1). Please notice that the formulas (A.2) are equivalent to the expressions (2.11) in the main body of the text.

To proceed, we record the formula [59, Tab. 5-2]

$$\langle \ell^n \rangle = \lambda^n \Gamma\left(1 + \frac{n}{k}\right), \quad n = 1, 2, 3, \dots, \quad (\text{A.4})$$

for the expectation of the n -th power of the length, the so-called n -th moment, of the Weibull distribution, involving Euler's Γ -function (2.13). To make use of this formula, we expand the variance (A.2) in terms of moments

$$\begin{aligned} \langle \ell \rangle s^2 &= \langle (\ell - m)^2 \ell \rangle = \langle (\ell^2 - 2m\ell + m^2) \ell \rangle \\ &= \langle \ell^3 - 2m\ell^2 + m^2 \ell \rangle = \langle \ell^3 \rangle - 2m \langle \ell^2 \rangle + m^2 \langle \ell \rangle, \end{aligned} \quad (\text{A.5})$$

using the linearity of the expectation (A.3), to arrive at the final expression

$$s^2 = \frac{\langle \ell^3 \rangle}{\langle \ell \rangle} - 2m \frac{\langle \ell^2 \rangle}{\langle \ell \rangle} + m^2 = \frac{\langle \ell^3 \rangle}{\langle \ell \rangle} - m^2, \tag{A.6}$$

where we used the formula (A.2) for the volume-weighted mean m . Invoking the formula (A.4) for the moments, we get the system

$$\begin{aligned} m &= \lambda \frac{\Gamma(1 + \frac{2}{k})}{\Gamma(1 + \frac{1}{k})} \\ s^2 &= \lambda^2 \frac{\Gamma(1 + \frac{3}{k})}{\Gamma(1 + \frac{1}{k})} - m^2 \end{aligned} \tag{A.7}$$

of equations. Solving for λ in the first equation

$$\lambda = m \frac{\Gamma(1 + \frac{1}{k})}{\Gamma(1 + \frac{2}{k})}. \tag{A.8}$$

and inserting this expression into the second equation yields the condition

$$\frac{\Gamma(1 + \frac{1}{k}) \Gamma(1 + \frac{3}{k})}{\Gamma(1 + \frac{2}{k})^2} - 1 = \frac{s^2}{m^2}. \tag{A.9}$$

The latter equation corresponds to Eq. (2.12), and condition (A.8) coincides with equation (2.14) in the main body of the text, as was to be shown.

Please note the Eq. (A.9) appears to be uniquely solvable for any given and positive right-hand side s^2/m^2 , see Fig. 12.

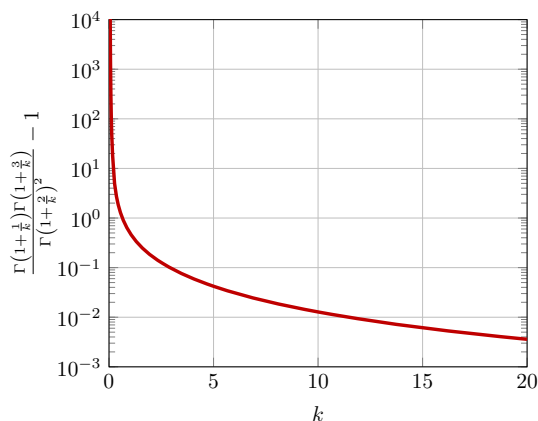


Fig. 12 Left-hand side of Eq. (A.9) to be solved. The function is strictly monotonically decreasing, converging to zeros as $k \rightarrow \infty$, and blows up as $k \rightarrow 0$

Appendix B Comparing the effective elastic moduli for the exact and the maximum-entropy closure

In this section, we would like to compare the exact closure approximation (2.20) to the maximum entropy closure (2.21). To separate the influence of the fiber-length distribution, we consider a uniform fiber-length distribution, with a length of $250\mu\text{m}$ and a diameter of $10\mu\text{m}$. Moreover, we consider PA6GF35, i.e., a commercial polyamide 6 with 35% (by weight) glass-fiber reinforcement. This corresponds to 19.3% filler content by volume. We use the material parameters given in Table 1, following Hessman et al. [40]. For the computations, we use the mesh and volume-element sizes identified in sect. 4, i.e., $h = 2\mu\text{m}$ and $Q = 600\mu\text{m}$.

To evaluate the differences between the closures, it is necessary to take a closer look at the set of possible input and output values of corresponding computations. The second-order fiber-orientation tensor A , see Eq. (2.18), serves as the input for the computations, whereas the effective stiffness \mathbb{C}^{eff} arises as the output. We would like to cover all possible input tensors A . For this purpose, we notice that any second-order fiber-orientation tensor may be written in the form

$$A = U \text{diag}(\lambda_1, \lambda_2, 1 - \lambda_1 - \lambda_2) U^T \tag{B.1}$$

with an orthogonal matrix $U \in \mathbb{R}^{3 \times 3}$ and a pair (λ_1, λ_2) of real numbers which satisfy the constraints

$$\lambda_1 \geq \lambda_2, \quad \lambda_1 + 2\lambda_2 \geq 1 \quad \text{and} \quad \lambda_1 + \lambda_2 \leq 1. \tag{B.2}$$

As an orthogonal transformation of the fiber-orientation tensor A leads to a suitable orthogonal transformation of the effective stiffness \mathbb{C}^{eff} it is actually sufficient to restrict attention to diagonal second-order tensors A which satisfy Eq. B.2. Geometrically, this phase space corresponds to a triangle in two dimensions, the fiber-orientation triangle [99].

The effective stiffness \mathbb{C}^{eff} depends continuously on the fiber-orientation tensor A , provided all other parameters remain fixed and the computational cells are sufficiently large to render the computations representative [26–28]. Therefore, it suffices to consider a (sufficiently fine) triangulation of the fiber-orientation triangle (B.2), which reduces the effort to a *finite* number of nodal computations. Here, we follow Köbler et al. [99] and consider a triangulation with 15 nodes and linear FE ansatz functions.

Regarding the output of the computations, working with the full stiffness tensor \mathbb{C}^{eff} , an object with 21 independent components, increases the difficulty in assessing the fine details. From an engineering perspective, it is more instructive to monitor the engineering constants associated to the effective stiffness. Indeed, for both the exact and the

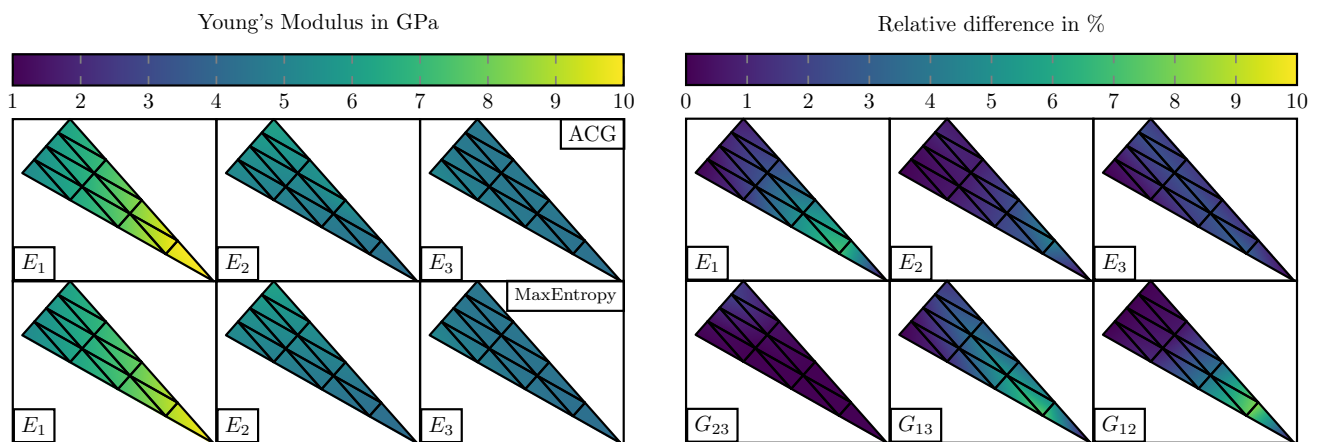


Fig. 13 Comparison between the exact closure (2.20) and the maximum entropy closure (2.21) on the fiber-orientation triangle [99]. We consider a composite with the properties listed in Tables 1 and 2

maximum entropy closure, the effective stiffness tensors are orthotropic. This is a direct consequence of the fact that every second-order tensor is orthotropic, in particular the second-order fiber-orientation tensor A , and the prescribed probability density functions (2.20) and (2.21) for both closures reflect this symmetry condition.

Thus, we report on the engineering constants of the effective stiffness, considered as functions on the fiber-orientation triangle. For the three directional Young's moduli, the results are shown in Fig. 13a. To the naked eye, both closures appear to give rise to almost identical results. This is a consequence of the following. For the three corners of the triangle, the unidirectional, the planar isotropic and the spatially isotropic fiber-orientation state, the fiber-orientation distributions for the maximum-entropy and the exact closure coincide. In particular, the effective elastic moduli coincide as well. Thus, the only possible differences arise in the interior of the fiber-orientation triangle.

To study these differences more closely, we investigate the *relative difference* between the engineering constants, where we take the exact closure as the reference. Fig. 13b shows the effective directional Young's moduli and the effective shear moduli for the three coordinate planes. The Young's modulus E_3 leads to the smallest difference between the closures among the directional Young's moduli, with a maximum difference of 3.1%. The difference for E_2 is only slightly larger at 4.6%. For E_1 , this difference increases to 7.1%. For all three moduli, these maximum differences are realized for $\lambda_1 \approx 0.8$. Yet, on average the difference is 2.6% for E_1 and at 1.3% and 1.6% for E_2 and E_3 , respectively.

Inspecting the shear moduli paints a similar picture - the moduli involving the 1-direction lead to larger differences than the shear modulus in the 2-3-plane. On average, the errors are 0.9%, 2.8% and 2.1% for G_{23} , G_{13} and G_{12} , respectively.

The maximum deviation is reached for G_{12} with 8.3% and $(\lambda_1, \lambda_2) = (7/8, 1/8)$.

References

- Mori T, Tanaka K (1973) Average stress in matrix and average elastic energy of materials with misfitting inclusions. *Acta Metallurgica* 21(5):571–574
- Willis JR (1981) Variational and related methods for the overall properties of composites. *Adv Appl Mech* 21:1–78
- Doghri I, Brassart L, Adam L, Gérard J-S (2011) A second-moment incremental formulation for the mean-field homogenization of elasto-plastic composites. *International J Plasticity* 27(3):352–371
- Matouš K, Geers MGD, Kouznetsova VG, Gillman A (2017) A review of predictive nonlinear theories for multiscale modeling of heterogeneous materials. *J Comput Phys* 330:192–220
- Kozlov SM (1978) "Averaging of differential operators with almost periodic rapidly oscillating coefficients," *Mathematics of the USSR-Sbornik*, vol. 107 (149), no. 2 (10), pp. 199–217
- Papanicolaou GC, Varadhan SRS (1981) "Boundary value problems with rapidly oscillating random coefficients," in *Random fields, Vol. I, II (Esztergom, 1979)*, vol. 27 of *Colloq. Math. Soc. János Bolyai*, pp. 835–873, North-Holland, Amsterdam-New York
- de Paiva RF, Bisiaux M, Lynch J, Rosenberg E (1996) High resolution x-ray tomography in an electron microprobe. *Rev Scientific Instruments* 67(6):2251–2256
- Shen H, Nutt S, Hull D (2004) Direct observation and measurement of fiber architecture in short fiber-polymer composite foam through micro-CT imaging. *Compos Sci Tech* 64(13–14):2113–2120
- Bargmann S, Klusemann B, Markmann J, Schnabel JE, Schneider K, Soyarslan C, Wilmers J (2018) Generation of 3D representative volume elements for heterogeneous materials: A review. *Progress Materials Sci* 96:322–384
- Widom B (1966) Random sequential addition of hard spheres to a volume. *J Chem Phys* 44(10):3888–3894
- Feder J (1980) Random sequential adsorption. *J Theor Biol* 87(2):237–254
- Evans KE, Gibson AG (1980) Prediction of the maximum packing fraction achievable in randomly oriented short-fibre composites. *Compos Sci Tech* 25:149–162

13. Toll S (1998) Packing mechanics of fiber reinforcements. *Polymer Eng Sci* 38(8):1337–1350
14. Tian W, Qi L, Zhou J, Liang J, Ma Y (2015) Representative volume element for composites reinforced by spatially randomly distributed discontinuous fibers and its applications. *Compos Struct* 131(7):366–373
15. Chen L, Gu B, Zhou J, Tao J (2019) Study of the Effectiveness of the RVEs for Random Short Fiber Reinforced Elastomer Composites. *Fibers and Polymers* 20(7):1467–1479
16. Tian W, Chao X, Fu MW, Qi L (2021) An advanced method for efficiently generating composite RVEs with specified particle orientation. *Compos Sci Tech* 205:108647
17. Li Z, Liu Z, Xue Y, Zhu P (2021) “A novel algorithm for significantly increasing the fiber volume fraction in the reconstruction model with large fiber aspect ratio,” *Journal of Industrial Textiles*, vol. accepted, pp. 1–25
18. Coelho D, Thovert J-F, Adler PM (1997) Geometrical and transport properties of random packings of spheres and aspherical particles. *Phys Rev E* 55(2):1959–1978
19. Pan Y, Iorga L, Pelegri AA (2006) Numerical generation of a random chopped fiber composite RVE and its elastic properties. *Compos Sci Tech* 68:56–66
20. Altendorf H, Jeulin D (2011) Random-walk-based stochastic modeling of three-dimensional fiber systems. *Phys Rev E* 83(4):041804
21. Altendorf H, Jeulin D, Willot F (2014) Influence of the fiber geometry on the macroscopic elastic and thermal properties. *International J Solids Struct* 51(23):3807–3822
22. Williams S, Philipse A (2003) Random packings of spheres and spherocylinders simulated by mechanical contraction. *Phys Rev E* 67(5):1–9
23. Pournin I, Weber M, Tsukahara M, Ferrez J-A, Ramaioli M, Liebling TM (2005) Three-dimensional distinct element simulation of spherocylinder crystallization. *Granular Matter* 7:119–126
24. Ghossein E, Lévesque M (2013) Random generation of periodic hard ellipsoids based on molecular dynamics: A computationally-efficient algorithm. *J Comput Phys* 253:471–490
25. Schneider M (2017) The Sequential Addition and Migration method to generate representative volume elements for the homogenization of short fiber reinforced plastics. *Comput Mech* 59:247–263
26. Hill R (1963) Elastic properties of reinforced solids: Some theoretical principles. *J Mech Phys Solids* 11(5):357–372
27. Drugan WJ, Willis JR (1996) A micromechanics-based nonlocal constitutive equations and estimates of representative volume element size for elastic composites. *J Mech Phys Solids* 44:497–524
28. Kanit T, Forest S, Galliet I, Mounoury V, Jeulin D (2003) Determination of the size of the representative volume element for random composites: statistical and numerical approach. *International J Solids Struct* 40(13–14):3647–3679
29. Köbler J, Magino N, Andrä H, Welschinger F, Müller R, Schneider M (2021) A computational multi-scale model for the stiffness degradation of short-fiber reinforced plastics subjected to fatigue loading. *Comput Methods Appl Mech Eng* 373:113522
30. Magino N, Köbler J, Andrä H, Welschinger F, Müller R, Schneider M (2022) A multiscale high-cycle fatigue-damage model for the stiffness degradation of fiber-reinforced materials based on a mixed variational framework. *Comput Methods Appl Mech Eng* 388:114198
31. Ernesti F, Schneider M (2021) A fast Fourier transform based method for computing the effective crack energy of a heterogeneous material on a combinatorially consistent grid. *International J Numer Methods Eng* 122(21):6283–6307
32. Ernesti F, Schneider M (2021) “Computing the effective crack energy of heterogeneous and anisotropic microstructures via anisotropic minimal surfaces,” *Computational Mechanics*, vol. Online, pp. 1–13
33. Wicht D, Schneider M, Böhlke T (2021) Computing the effective response of heterogeneous materials with thermomechanically coupled constituents by an implicit FFT-based approach. *International J Numer Methods Eng* 122(5):1307–1332
34. Gajek S, Schneider M, Böhlke T (2022) “An FE-DMN method for the multiscale analysis of thermomechanical composites,” *Computational Mechanics*, vol. Online, pp. 1–27
35. Hessman PA, Riedel T, Welschinger F, Hornberger K, Böhlke T (2019) Microstructural analysis of short glass fiber reinforced thermoplastics based on x-ray micro-computed tomography. *Compos Sci Tech* 183:107752
36. Robb K, Wirjadi O, Schladitz K (2007) “Fiber orientation estimation from 3D image data: Practical algorithms, visualization, and interpretation,” In: *Proceedings of the International Conference on Hybrid Intelligent Systems, (Kaiserslautern)*, pp. 320–325, IEEE
37. Wirjadi O, Schladitz K, Rack A, Breuel T (2009) “Applications of anisotropic image filters for computing 2d and 3d-fiber orientations,” In: *Proceedings of the 10th European Congress on Stereology and Image Analysis, (Milano)*, pp. 1–6, Esculapio
38. Krause M, Hausherr JM, Burgeth B, Herrmann C, Krenkel W (2010) Determination of the fibre orientation in composites using the structure tensor and local X-ray transform. *J Mater Sci* 45:888–896
39. Goris S, Back T, Yanev A, Brands D, Drummer D, Osswald TA (2018) A novel fiber length measurement technique for discontinuous fiber-reinforced composites: A comparative study with existing methods. *Polymer Compos* 39:4058–4070
40. Hessman PA, Welschinger F, Hornberger K, Böhlke T (2021) On mean field homogenization schemes for short fiber reinforced composites: Unified formulation, application and benchmark. *International J Solids Struct* 230–231:111141
41. Weibull W (1951) A statistical distribution function of wide applicability. *J Appl Mech* 18(3):293–297
42. Fu S-Y, Lauke B (1996) Effects of fiber length and fiber orientation distributions on the tensile strength of short-fiber-reinforced polymers. *Compos Sci Tech* 56:1179–1190
43. Fu S-Y, Hu X, Yue C-Y, Mai Y-W (1999) Effects of fiber length and orientation distributions on the mechanical properties of short-fiber-reinforced polymers. A review. *Mater Sci Res International* 5(2):74–83
44. Fu S-Y, Yue C-Y, Hu X, Mai Y-W (2001) Characterization of fiber length distribution of short-fiber reinforced thermoplastics. *J Mater Sci Lett* 20:31–33
45. Kanatani K (1984) Distribution of directional data and fabric tensors. *International J Eng Sci* 22:149–164
46. Advani SG, Tucker CL (1987) The Use of Tensors to Describe and Predict Fiber Orientation in Short Fiber Composites. *J Rheology* 31:751–784
47. Altendorf H, Jeulin D (2009) 3d directional mathematical morphology for analysis of fiber orientations. *Image Anal Stereol* 28:143–153
48. Pinter P, Dietrich S, Bertram B, Kehler L, Elsner P, Weidenmann KA (2018) Comparison and error estimation of 3D fibre orientation analysis of computed tomography image data for fibre reinforced composites. *NDT and E International* 95:26–35
49. Folgar F, Tucker CL III (1984) Orientation behaviour of fibers in concentrated suspensions. *J Reinforced Plastics Compos* 3:98–119
50. Kennedy P, Zheng R (2013) *Flow Analysis of Injection Molds*. Munich: Hanser, second ed
51. Wirjadi O, Schladitz K, Easwaran P, Ohser J (2016) Estimating fibre direction distributions of reinforced composites from tomographic images. *Image Analysis & Stereology* 35(3):167–179
52. Eberhardt CN, Clarke AR (2002) Automated reconstruction of curvilinear fibres from 3D datasets acquired by X-ray microtomography. *J Microscopy* 206(1):41–53

53. Salaberger D, Kannappan KA, Kastner J, Reussner J, Auinger T (2011) Evaluation of computed tomography data from fibre reinforced polymers to determine fibre length distribution. *International Polymer Process* 26(3):283–291
54. Glöckner R, Kolling S, Heiliger C (2016) A Monte-Carlo Algorithm for 3D Fibre Detection from Microcomputer Tomography. *J Comput Eng* 2016:2753187
55. Breuer K, Stommel M (2020) RVE modelling of short fiber reinforced thermoplastics with discrete fiber orientation and fiber length distribution. *SN Appl Sci* 2:91
56. Cintra JS, Tucker CL III (1995) Orthotropic closure approximations for flow-induced fiber orientation. *J Rheology* 39(6):1095–1122
57. Chaubal CV, Leal L (1998) A closure approximation for liquid-crystalline polymer models based on parametric density estimation. *J Rheology* 42(1):177
58. Kugler SK, Kech A, Cruz C, Osswald T (2020) Fiber Orientation Predictions - A Review of Existing Models. *J Compos Sci* 4(2):69
59. Papoulis AP, Unnikrishna Pillai S (2002) *Probability, Random Variables, and Stochastic Processes*. Boston: McGraw-Hill, fourth ed
60. Müller V, Böhlke T (2016) Prediction of effective elastic properties of fiber reinforced composites using fiber orientation tensors. *Compos Sci Tech* 130:36–45
61. Schneider M (2021) “An algorithm for generating microstructures of fiber-reinforced composites with long fibers,” *International Journal for Numerical Methods in Engineering*, vol. Submitted, pp. 1–27
62. Breuer K, Stommel M, Korte W (2019) Analysis and Evaluation of Fiber Orientation Reconstruction Methods. *J Compos Sci* 3(3):67
63. Breuer K, Spickenheuer A, Stommel M (2021) Statistical Analysis of Mechanical Stressing in Short Fiber Reinforced Composites by Means of Statistical and Representative Volume Elements. *Fibers* 9(5):32
64. Montgomery-Smith S, He W, Jack D, Smith D (2011) Exact tensor closures for the three-dimensional Jeffery’s equation. *J Fluid Mech* 680:321–335
65. Montgomery-Smith S, Jack D, Smith DE (2011) The Fast Exact Closure for Jeffery’s equation with diffusion. *J Non-Newtonian Fluid Mech* 166:343–353
66. Tyler DE (1987) Statistical Analysis for the Angular Central Gaussian Distribution on the Sphere. *Biometrika* 74(3):579–589
67. Verley V, Dupret F (1994) Numerical prediction of the fiber orientation in complex injection molded parts. *Trans Eng Sci* 4:303–312
68. Bingham C (1974) An antipodally symmetric distribution on the sphere. *Ann Stat* 2:1201–1225
69. Ospald F, Herzog R (2020) “Short note on a relation between the inverse of the cosine and Carlson’s elliptic integral R_D ,” [arXiv:2001.02203](https://arxiv.org/abs/2001.02203), pp. 1–7
70. Carlson BC (1995) Numerical computation of real or complex elliptic integrals. *Numerical Algorithms* 10:13–26
71. Görthofer J, Schneider M, Ospald F, Hrymak A, Böhlke T (2020) Computational homogenization of sheet molding compound composites based on high fidelity representative volume elements. *Comput Mater Sci* 174:109456
72. Ospald F, Goldberg N, Schneider M (2017) A fiber orientation-adapted integration scheme for computing the hyperelastic Tucker average for short fiber reinforced composites. *Comput Mech* 60(4):595–611
73. Womersley RS (2018) *Efficient Spherical Designs with Good Geometric Properties*. Springer, Cham, pp 1243–1285
74. Hammersley JM, Handscomb DC (1964) *Monte Carlo Methods*. Chapman and Hall, London
75. Calfisch RE (1998) Monte Carlo and quasi-Monte Carlo methods. *Acta Numerica* 7:1–49
76. Dick J, Pillichshammer F (2010) *Digital Nets and Sequences*. Cambridge University Press, Discrepancy Theory and Quasi-Monte Carlo Integration. Cambridge
77. Owen AB (1995) “Randomly Permuted (t,m,s)-Nets and (t, s)-Sequences,” In: *Monte Carlo and Quasi-Monte Carlo Methods in Scientific Computing* (H. Niederreiter and P. J.-S. Shiue, eds.), (New Yor), pp. 299–317, Springer
78. Sobol IM (1967) On the distribution of points in a cube and the approximate evaluation of integrals. *USSR Comput Math and Math Phys* 7(4):86–112
79. Sobol IM (1967) Uniformly distributed sequences with additional uniformity properties. *USSR Comput Math and Math Phys* 16:236–242
80. Paszke, A, Gross S, Chintala S, Chanan G, Yang E, DeVito Z, Lin Z, Desmaison A, Antiga L, Lerer A (2017) “Automatic Differentiation in PyTorch,” In: *NIPS Autodiff Workshop*,
81. Schneider M (2019) On the Barzilai-Borwein basic scheme in FFT-based computational homogenization. *International J Numer Methods Eng* 118(8):482–494
82. Schneider M, Wicht D, Böhlke T (2019) On polarization-based schemes for the FFT-based computational homogenization of inelastic materials. *Comput Mech* 64(4):1073–1095
83. Schneider M, Ospald F, Kabel M (2016) Computational homogenization of elasticity on a staggered grid. *International J Numer Methods Eng* 105(9):693–720
84. Zeman J, Vondřejc J, Novák J, Marek I (2010) Accelerating a FFT-based solver for numerical homogenization of periodic media by conjugate gradients. *J Comput Phys* 229(21):8065–8071
85. Brisard S, Dormieux L (2010) FFT-based methods for the mechanics of composites: A general variational framework. *Comput Mater Sci* 49(3):663–671
86. Schneider M (2020) A dynamical view of nonlinear conjugate gradient methods with applications to FFT-based computational micromechanics. *Comput Mech* 66:239–257
87. Schneider M (2021) A review of non-linear FFT-based computational homogenization methods. *Acta Mech* 232:2051–2100
88. Cowin SC (1985) The relationship between the elasticity tensor and the fabric tensor. *Mech Mater* 4(2):137–147
89. Brisard S, Dormieux L (2012) Combining Galerkin approximation techniques with the principle of Hashin and Shtrikman to derive a new FFT-based numerical method for the homogenization of composites. *Comput Methods Appl Mech Eng* 217–220:197–212
90. Schneider M (2015) Convergence of FFT-based homogenization for strongly heterogeneous media. *Math Methods Appl Sci* 38(13):2761–2778
91. Ye C, Chung ET (2022) “Numerical analysis of several FFT-based schemes for computational homogenization,” [arXiv:2201.01916](https://arxiv.org/abs/2201.01916), pp. 1–17
92. Doškář M, Zeman J, Jarušková D, Novák J (2018) Wang tiling aided statistical determination of the Representative Volume Element size of random heterogeneous materials. *Eur J Mech - A/Solids* 70:280–295
93. Dirrenberger J, Forest S, Jeulin D (2014) Towards gigantic RVE sizes for 3D stochastic fibrous networks. *International J Solids Struct* 51(2):359–376
94. Jeulin D (2016) Power Laws Variance Scaling of Boolean Random Varieties. *Methodol Comput Appl Probab* 18(4):1065–1079
95. Gloria A, Otto F (2011) An optimal variance estimate in stochastic homogenization of discrete elliptic equations. *The Ann probab* 39(3):779–856
96. Sab K, Nedjar B (2005) Periodization of random media and representative volume element size for linear composites. *C R Mécanique* 333(2):187–195
97. Schneider M, Josien M, Otto F (2022) Representative volume elements for matrix-inclusion composites - a computational study on the effects of an improper treatment of particles intersecting the

- boundary and the benefits of periodizing the ensemble. *J Mech Phys Solids* 158:104652
98. Bernasconi A, Cosmi F, Dreossi D (2008) Local anisotropy analysis of injection moulded fibre reinforced polymer composites. *Compos Sci Tech* 68:2574–2581
99. Köbler J, Schneider M, Ospald F, Andrä H, Müller R (2018) Fiber orientation interpolation for the multiscale analysis of short fiber reinforced composite parts. *Comput Mech* 61(6):729–750

Publisher's Note Springer Nature remains neutral with regard to jurisdictional claims in published maps and institutional affiliations.